Galaxy–galaxy weak gravitational lensing in $f(R)$ gravity

Baojiu Li[1]★ and Masato Shirasaki[2]★

[1]*Institute for Computational Cosmology, Department of Physics, Durham University, South Road, Durham DH1 3LE, UK*
[2]*Division of Theoretical Astronomy, National Astronomical Observatory of Japan, 2-21-1 Osawa, Mitaka, Tokyo 181-8588, Japan*

ABSTRACT

We present an analysis of galaxy–galaxy weak gravitational lensing (GGL) in chameleon $f(R)$ gravity – a leading candidate of non-standard gravity models. For the analysis, we have created mock galaxy catalogues based on dark matter haloes from two sets of numerical simulations, using a halo occupation distribution (HOD) prescription which allows a redshift dependence of galaxy number density. To make a fairer comparison between the $f(R)$ and Λ cold dark matter (ΛCDM) models, their HOD parameters are tuned so that the galaxy two-point correlation functions in real space (and therefore the projected two-point correlation functions) match. While the $f(R)$ model predicts an enhancement of the convergence power spectrum by up to $\sim$30 per cent compared to the standard ΛCDM model with the same parameters, the maximum enhancement of GGL is only half as large and less than 5 per cent on separations above $\sim$1–2 h^{-1} Mpc, because the latter is a cross-correlation of shear (or matter, which is more strongly affected by modified gravity) and galaxy (which is weakly affected given the good match between galaxy autocorrelations in the two models) fields. We also study the possibility of reconstructing the matter power spectrum by combination of GGL and galaxy clustering in $f(R)$ gravity. We find that the galaxy–matter cross-correlation coefficient remains at unity down to $\sim$2–3 h^{-1} Mpc at relevant redshifts even in $f(R)$ gravity, indicating joint analysis of GGL and galaxy clustering can be a powerful probe of matter density fluctuations in chameleon gravity. The scale dependence of the model differences in their predictions of GGL can potentially allows us to break the degeneracy between $f(R)$ gravity and other cosmological parameters such as $\Omega_{\rm m}$ and σ_8.

Key words: gravitational lensing: weak – methods: numerical – dark energy – large-scale structure of Universe – cosmology: theory.

1 INTRODUCTION

One of the key, unanswered, questions in modern cosmology is the accelerated expansion rate of our Universe. Since its discovery almost 20 yr ago (Riess et al. 1998; Perlmutter et al. 1999), it has been confirmed by various other observations, leading to the establishment of the concordance Λ cold dark matter (ΛCDM) model, in which the Universe is dominated by a small cosmological constant Λ which is solely responsible for the accelerated expansion at late times, while the formation of its structures has largely been shaped by dark matter component under the action of gravity, which is assumed to be described by Einstein's General Relativity (GR). While the simple ΛCDM model describes almost all cosmological observations very well (WMAP Collaboration 2013; Planck Collaboration XIII 2016), currently there still lacks a satisfactory theoretical explanation for the smallness of Λ required by observa-

tions, and this has led to significant effort in developing alternative scenarios, such as those which assume that GR is inaccurate and must be replaced by some modified gravity (MG) model on cosmological scales (see e.g. Joyce et al. 2015; Koyama 2016, for recent reviews). Although a commonly accepted MG model still does not exist, and many of the MG models being proposed indeed introduce a Λ through back door, studies in this field have so far led to various interesting possibilities of deviations from GR, which serve as useful testbeds of the validity of GR in cosmology. In recent and coming years, various imaging and spectroscopic galaxy surveys are producing high-quality data for a range of cosmological probes, with which we can hope to improve our understanding of the nature of the cosmic acceleration, along which it is hopeful to push the test of GR to much larger scales than previously attained.

Weak gravitational lensing (Bartelman & Schneider 2001; Refregier 2003; Hoekstra & Jain 2008; Kilbinger 2015) is one of the key cosmological probes that such galaxy surveys offer. It describes the effect that images of distant sources (e.g. galaxies or the cosmic microwave background itself) are distorted by the

★ E-mail: baojiu.li@durham.ac.uk (BL); masato.shirasaki@nao.ac.jp (MS)

intervening large-scale structures, which bend the paths of the photons emitted by the sources. Such bending is caused by visible plus dark matter, so that weak lensing offers a venue to detect the total matter distribution between the source and observer. Weak lensing can be observed in different ways, depending on the size of the lensing objects. At one extreme, the lensing effect by the largest bound objects in the Universe – galaxy clusters – is strong enough that it can be detected around individual clusters. At the other extreme, cosmic shear describes statistically the lensing effect of the entire matter distribution along the lines of sight. Other objects, such as cosmic voids and galaxies, produce lensing signals which are most often not strong or clean enough to allow a clear detection for individual lenses. However, with the stacking of a large number of lenses, a signal can be extracted and it can tell us how matter is distributed around such objects. In this paper, we will focus on the lensing of background (source) galaxies by foreground (lens) galaxies, or galaxy–galaxy lensing (GGL; Brainerd, Blandford & Smail 1996; Hudson et al. 1998; Guzik & Seljak 2002; Hoekstra, Yee & Gladders 2004; Mandelbaum et al. 2006; Clampitt et al. 2017). For some recent works on testing cosmological models with cluster or void lensing, see Cai, Padilla & Li (2015), Cautun et al. (2017), and Barreira et al. (2015a,b, 2017).

As a *gravitational* effect, weak *gravitational* lensing can naturally be used to test *gravitational* physics. On cosmological scales, a deviation from standard GR can leave detectable imprints on lensing observations in various ways. For example, it could change the expansion history through a different mechanism than Λ to accelerate the expansion or via different best-fitting cosmological parameters such as Ω_m and H_0, leading to different angular diameter distances to lenses and sources at given redshifts. It may have a different law of gravitational interaction, enhancing or reducing the clustering of matter at cosmological scales. It may also affect the propagation of photons, such as in the Galileon (Nicolis, Rattazzi & Trincherini 2009; Deffayet, Esposito-Farese & Vikman 2009), non-local (Maggiore & Mancarella 2014; Dirian et al. 2014), and beyond Horndeski (Glayzes et al. 2015) gravity models. These effects, unfortunately, can have certain degeneracies between each other (and degenerate with the effects of cosmological parameters such as Ω_m and σ_8), and in this paper we focus on a simple model – chameleon $f(R)$ gravity – which practically does not modify the expansion history and photon propagation. This is one of the most popular classes of MG models, which has the property of chameleon screening (Khoury & Weltman 2004; Mota & Shaw 2007) to suppress the deviation from GR in regions of deep gravitational potential (such as our Solar system) and ensure that the theory passes local tests of gravity.

The study of GGL in chameleon $f(R)$ gravity presented here is based on numerical simulations. Instead of doing a ray tracing to calculate the stacked lensing signal around galaxies, we will follow an equivalent approach by integrating the cross-correlation function $\xi_{gm}(r)$ of galaxies and matter along the line of sight (los). The calculation is standard, but a significant effort of this study will be devoted to the construction of mock galaxy catalogues used to find $\xi_{gm}(r)$. The reason for this carefulness is twofold. First, galaxies are observable and biased tracers of the underlying matter density field, and different populations of galaxies have different biases and density profiles around them. Therefore, it is important to know which galaxy population in observations should our simulation prediction of GGL signal be confronted to. Secondly (and which has perhaps not been emphasized enough so far), there is only one observable Universe, while there are many theories. For probes such as GGL, which involve the distributions of both source galaxies and the total

matter field, the difference between the predictions of two models can come from differences in both. If, say, two models predict very different clustering of foreground galaxies, then one of them may already be incompatible with the spectroscopic observation used to identify these lenses, and the comparison of its GGL prediction to observations no longer makes sense. Of course, given the complex and poorly understood galaxy-mass and galaxy-halo connection, at this point it is premature to rule out the models studied here purely based on their predicted galaxy clustering. For example, commonly adopted frameworks to populate galaxies into simulations, such as halo occupancy distribution (HOD), abundance matching (SHAM), and semi-analytical modelling (SAM), usually have or can accept enough free parameters by tuning which the predicted and observed galaxy clustering can be matched (as we shall show below). Therefore, in this work, we follow a pragmatic approach, by assuming that we have no idea whether GR or $f(R)$ gravity is the correct theory, and that for both of them the free parameters of the HOD (which we use to make galaxy mocks) can be tuned to produce acceptable clustering properties of the resulting galaxy catalogues, which will then be used to make predictions of GGL.

The layout of this paper is as follows. In Section 2, we present a short description of the $f(R)$ gravity model studied here, a concise summary of weak gravitational lensing and GGL, and a detailed discussion of our numerical simulations and mock HOD galaxy catalogues. In Section 2.2, we present the main results of this paper, including the power spectrum of cosmic shear, cross-correlation between galaxies and matter, galaxy bias, and GGL in both GR and $f(R)$ gravity. We will also present a forecast of the potential to distinguish the two models using cosmic shear and GGL, for galaxy surveys such as Dark Energy Survey (DES Dark Energy Survey Collaboration et al. 2016),[1] the Hyper Supreme Camera (HSC; Aihara et al. 2017),[2] and Large Synoptic Survey Telescope (LSST; Ivezic et al. 2008).[3] Finally, in Section 4, we sum up and discuss potential ways in which this work can be further improved.

Throughout this paper, we use the unit convention $c = 1$ where c is the speed of light. An overbar denotes the background value, and a subscript $_0$ denotes the present-day value, of a quantity. Greek indices $\mu, \nu, \ldots$ run over 0, 1, 2, 3 (space–time coordinates) while Latin indices $i, j, k, \ldots$ run over 1, 2, 3 (space coordinates only). The Einstein summation convention is used across the paper unless otherwise stated. Also, we only consider a spatially flat universe.

2 THE THEORETICAL FRAMEWORK

We start with a concise description of $f(R)$ gravity and the model studied in this paper (Section 2.1), the formulae of weak gravitational lensing (Section 2.2), and the N-body simulations used in the analyses and the catalogues of HOD galaxies which are needed to study their cross-correlation with lensing (Section 2.3).

2.1 The $f(R)$ gravity theory

2.1.1 Generic $f(R)$ gravity

$f(R)$ gravity as an attempt to explain the accelerated late-time expansion of the Universe without invoking a cosmological constant was first proposed in Carroll et al. (2004, 2005). It is constructed by

---

[1] https://www.darkenergysurvey.org

[2] http://hsc.mtk.nao.ac.jp/ssp/

[3] https://www.lsst.org

replacing the Ricci scalar R in the standard Einstein–Hilbert action for GR with a function of R, $f(R)$:

$$S = \int \mathrm{d}^4x \sqrt{-g} \, \frac{1}{2} M_{\mathrm{Pl}}^2 \left[R + f(R) \right], \qquad (1)$$

in which M_{Pl} is the reduced *Planck* mass, with $M_{\mathrm{Pl}}^{-2} = 8\pi G$ and G being Newton's constant, g is the determinant of the metric $g_{\mu\nu}$. The above is the gravitational action; the matter part is assumed to be the same as in standard ΛCDM, and so not explicitly given here.

A modified version of the Einstein equation can be derived by varying the action equation (1) with respect to the metric $g_{\mu\nu}$:

$$G_{\mu\nu} + f_R R_{\mu\nu} + \left[\Box f_R - \frac{1}{2} f \right] g_{\mu\nu} - \nabla_\mu \nabla_\nu f_R = 8\pi G T_{\mu\nu}. \qquad (2)$$

where $G_{\mu\nu} \equiv R_{\mu\nu} - \frac{1}{2} g_{\mu\nu} R$ is the Einstein tensor, ∇_μ the covariant derivative, $f_R \equiv \mathrm{d}f/\mathrm{d}R$ is a (new) scalar degree of freedom in this theory, $\Box \equiv \nabla^\alpha \nabla_\alpha$ the Laplancian, and $T_{\mu\nu}$ the energy-momentum tensor for matter.

Equation (2) is a fourth-order equation in the metric tensor because the Ricii scalar R itself contains second-order derivatives of the latter. It is convenient to cast it into a form involving the usual Einstein equation in GR plus the new scalar field (sometimes called the scalaron) f_R. The Klein–Gordon equation for f_R can be derived as the trace of the modified Einstein equation:

$$\Box f_R = \frac{1}{3} \left[R - f_R R + 2f + 8\pi G \rho_{\mathrm{m}} \right], \qquad (3)$$

in which ρ_{m} is the density for non-relativistic matter. We have neglected the contribution of relativistic matter species in this paper because we will focus on late times only.

The analysis in this study will be restricted to length-scales much smaller than the horizon, in which case we can use the quasi-static approximation to drop all time derivatives of f_R as compared with their spatial derivatives (see e.g. Bose, Hellwing & Li 2015, for a detailed discussion of this approximation). As a result of this simplification, equation (3) becomes

$$\vec{\nabla}^2 f_R = -\frac{1}{3} a^2 \left[R(f_R) - \bar{R} + 8\pi G (\rho_{\mathrm{m}} - \bar{\rho}_{\mathrm{m}}) \right], \qquad (4)$$

where $\vec{\nabla}$ is the spatial gradient and a the scale factor ($a = 1$ today).

Also under the quasi-static and weak-field approximation, the Poisson equation that governs the Newtonian potential Φ is modified:

$$\vec{\nabla}^2 \Phi = \frac{16\pi G}{3} a^2 (\rho_{\mathrm{m}} - \bar{\rho}_{\mathrm{m}}) + \frac{1}{6} \left[R(f_R) - \bar{R} \right]. \qquad (5)$$

The scalar field is what mediates a fifth force between massive particles in $f(R)$ gravity, and f_R plays the role of its potential. To see this, we can combine equations (4) and (5) to obtain the following equation:

$$\vec{\nabla}^2 \Phi = 4\pi G a^2 (\rho_{\mathrm{m}} - \bar{\rho}_{\mathrm{m}}) + \frac{1}{2} \vec{\nabla}^2 f_R. \qquad (6)$$

Equation (6) makes explicit the behaviour of the theory in the limit when $|f_R| \ll |\Phi|$: here we can to a good approximation neglect the effect of f_R and recover the usual Poisson equation

$$\vec{\nabla}^2 \Phi = 4\pi G \delta\rho_{\mathrm{m}}, \qquad (7)$$

in which $\delta\rho_{\mathrm{m}} \equiv \rho_{\mathrm{m}} - \bar{\rho}_{\mathrm{m}}$ is the matter density perturbation. The GR solution $R = -8\pi G \rho_{\mathrm{m}}$ is also recovered in this regime, where the fifth force is effectively suppressed, as the consequence of the so-called chameleon screening mechanism (Khoury & Weltman 2004; Mota & Shaw 2007).

As the opposite limit, when $|f_R| \geq |\Phi|$, we have $|\delta R| \ll \delta\rho_{\mathrm{m}}$ with $\delta R \equiv R - \bar{R}$, and so the second term on the right-hand side of the modified Poisson equation, equation (5), can be neglected:

$$\vec{\nabla}^2 \Phi \approx \frac{16}{3} \pi G \delta\rho_{\mathrm{m}}. \qquad (8)$$

Compare this with equation (6), we can notice a 1/3 enhancement of the strength of gravity, independent of the functional form of $f(R)$. The exact form of $f(R)$, though, determines the transition between the two limiting regimes. We shall call these two regimes, respectively, the *screened* and *unscreened* regimes.

We can see that the chameleon mechanism works depending on the local Newtonian potential Φ, and it efficiently screens the fifth force in environments where Φ is deep (i.e. $|\Phi| \gg |f_R|$). This can be qualitatively understood as follows: the fifth force is mediated by the scalar field f_R, which has a mass m_{s} given by

$$m_{\mathrm{s}}^2 = \frac{\mathrm{d}^2 V_{\mathrm{eff}}(f_R)}{\mathrm{d}f_R^2}, \qquad (9)$$

where the effective potential $V_{\mathrm{eff}}(f_R)$, due to the self-interaction of the scalar field and its interactions with (non-relativistic) matter, is given by

$$\frac{\mathrm{d}V_{\mathrm{eff}}(f_R)}{\mathrm{d}f_R} = \frac{1}{3} \left[R - f_R R + 2f + 8\pi G \rho_{\mathrm{m}} \right]. \qquad (10)$$

As a result of $m_{\mathrm{s}} \neq 0$ in general, the fifth force mediated by f_R has the Yukawa form, with a potential $\sim r^{-1} \exp(-m_{\mathrm{s}} r)$, where r is the distance from a massive particle. The complicated form of $V_{\mathrm{eff}}(f_R)$ makes m_{s} dependent on environment, and becomes heavy in deep Φ, where the Yukawa force decays very quickly with distance, such that its effect is not felt beyond $\sim m_{\mathrm{s}}^{-1}$. This is the origin of the chameleon screening, and this property can help the theory to pass stringent Solar system tests, since it is expected that screening has effectively suppressed the fifth force to an undetected level at locations where such tests have been performed.

2.1.2 The choice of f(R) model

The requirement of chameleon screening be in place for the model to pass Solar system tests does not significantly constrain the possible functional form of $f(R)$. As a result, many different forms have been studied in the literature with differing details. While many of these are interesting, in practice it is both impossible and unnecessary to study all of them with equal detail. Instead, there are reasons why we should focus on a particular example which is to be studied in greater details.

First, there is currently not a fundamental theory to naturally motivate a functional form of $f(R)$ that leads to the cosmic acceleration, and therefore all choices of $f(R)$ used in the literature so far are phenomenological. There is no clear reason why any choice should be preferred over the others, apart from possibly an apparent simplicity in the functional form of $f(R)$. However, it is known that for general $f(R)$ models that realize an efficient chameleon screening, the background expansion history has to be very close to that of ΛCDM (e.g. Brax et al. 2008; Wang, Hui & Khoury 2012; Ceron-Hurtado, He & Li 2016); in other words, a Λ is usually introduced to the theory, possibly in an implicit way, regardless of the simplicity of $f(R)$.

Second, as mentioned above, the different $f(R)$ models generally share some common features, such as chameleon screening in deep Newtonian potentials, and differ primarily in how efficient the screening is. However, given a functional form of $f(R)$, the screening

efficiency also depends on the parameter used. At least qualitatively, the change of behaviours by varying the form of $f(R)$ can be mimicked by varying the parameters with a chosen $f(R)$. Instead of letting observations determine the form of $f(R)$, it is pragmatically more useful to use observations to determine to what extent deviations from GR as prescribed by $f(R)$ gravity are allowed. The latter task can be carried out by working on a particular model which is to be tested against as many observational data sets as possible, as precisely as possible.

For these reasons, this work is based on the model proposed by Hu & Sawicki (2007, hereafter HS). This is the most well-studied example of $f(R)$ gravity, so that the results of this paper will be built upon various existing tests of this model. The particular functional form of $f(R)$ in this model makes it possible to implement an efficient algorithm to speed up simulations of it (Bose et al. 2017), which we adopt for the simulations used in this work. Additionally, this model is a representative example of classes of scalar-tensor-type MG theories, in that by varying its parameters we can have a range of behaviours ranging from strong screening to no screening.

The HS model has the following functional form of $f(R)$,

$$f(R) = -\frac{c_1 \left(-R/M^2\right)^n}{1 + c_2 \left(-R/M^2\right)^n} M^2, \tag{11}$$

where M is a parameter of mass dimension that is given by $M^2 \equiv 8\pi G \bar{\rho}_{m0}/3 = H_0^2 \Omega_m$, H the Hubble rate, Ω_m the present-day density parameter for non-relativistic matter, and c_1, c_2 are dimensionless model parameters.

In the limit $|\bar{R}| \gg M^2$, $\bar{f} \equiv f(\bar{R})$ is approximately a constant $-\frac{c_1}{c_2}M^2$, so that f_R and its derivatives are small. In this case, equation (3) can be simplified as

$$-\bar{R} \approx -2\bar{f} + 8\pi G\bar{\rho}_m \approx 3M^2 \left[\frac{2c_1}{3c_2} + a^{-3}\right]. \tag{12}$$

The background expansion rate is therefore close to that of ΛCDM, if we make mapping $\frac{c_1}{c_2} = 6\frac{\Omega_\Lambda}{\Omega_m}$, where $\Omega_\Lambda \equiv 1 - \Omega_m$. For $\Omega_\Lambda \sim 0.7$ and $\Omega_m \sim 0.3$, we have $|\bar{R}| \sim 40M^2 \gg M^2$ today. As $|\bar{R}|$ increases with redshift, the approximation in equation (12) is good all the time. In this approximation, we have the following simplified relation between f_R and R,

$$f_R \approx -n\frac{c_1}{c_2^2}\left(\frac{M^2}{-R}\right)^{n+1}. \tag{13}$$

This relation can be inverted to find $R(f_R)$, as the latter appears in field equations. Therefore, with choices of n and c_1/c_2^2, as well as Ω_m, Ω_Λ, H_0, an $f(R)$ model can be fully specified. In the literature, instead of c_1/c_2^2, people usually use f_{R0}, the current value of f_R, as the model parameter. We have

$$\frac{c_1}{c_2^2} = -\frac{1}{n}f_{R0}\left[3\left(1 + 4\frac{\Omega_\Lambda}{\Omega_m}\right)\right]^{n+1}. \tag{14}$$

In this paper, we shall focus on a particular choice of model parameters: $n = 1$ and $f_{R0} = -10^{-5}$, which we refer to as F5. This choice of f_{R0} is almost certainly incompatible with local gravity tests as the Milky Way galaxy is unlikely to be screened. However, the choice is not yet completely ruled out by cosmological observations, and for the GGL analysis we would like to choose a model that can maximize the difference from GR (see e.g. Cai, Padilla & Li 2015; Cataneo et al. 2015; Liu et al. 2016; Shirasaki, Hamana & Yoshida 2016; Shirasaki et al. 2017; Peirone et al. 2017; Cautun et al. 2017, for some recent studies on the current and potential constraints $f(R)$ gravity).

2.2 Weak gravitational lensing

Weak lensing is a matured field with a huge body of research works in the literature (see e.g. Bartelman & Schneider 2001; Hoekstra & Jain 2008; Kilbinger 2015, for some reviews). Here, we only give a very quick catch-up of some essential equation to be used in the discussion below. For simplicity, we assume a flat Universe.

As photons pass through the large-scale structure in the Universe, their paths are bent by the latter, resulting in a change of their apparent angular position $\vec{\xi}_0 \equiv \vec{\xi}(\chi = 0)$ as seen by the observer at today (where χ is the comoving distance), as compared to the true one $\vec{\xi}_s \equiv \vec{\xi}(\chi_s)$, at the source (where χ_s is the comoving distance to the source). This is given by

$$\vec{\xi}_0 - \vec{\xi}_s = 2\int_0^{\chi_s} \frac{g(\chi,\chi_s)}{\chi^2}\vec{\nabla}_{\vec{\xi}}\Phi d\chi, \tag{15}$$

where

$$g(\chi,\chi_s) \equiv \frac{\chi}{\chi_s}(\chi_s - \chi), \tag{16}$$

is the lensing kernel, and $\Phi \equiv \Phi(\chi, \vec{\xi})$ is the lensing potential along the los, and $\vec{\nabla}_{\vec{\xi}}$ is the 2D derivative in the plane perpendicular to the los. The resulting distortions of source images can be described by a 2×2 distortion matrix given by

$$A_{ij} = \delta_{ij} - 2\int_0^{\chi_s} \frac{g(\chi,\chi_s)}{\chi^2}\nabla_{\xi_{0,i}}\nabla_{\xi_j}\Phi(\chi,\vec{\xi})d\chi,$$

$$\approx \delta_{ij} - 2\int_0^{\chi_s} \frac{g(\chi,\chi_s)}{\chi^2}\nabla_{\xi_i}\nabla_{\xi_j}\Phi(\chi,\vec{\xi})d\chi, \tag{17}$$

where $i, j = 1, 2$, δ_{ij} is the Kronecker delta, $\nabla_{\xi_{0,i}}$ and ∇_{ξ_i} are, respectively, the derivative with respect to ξ_i at $\chi = 0$ and χ. We have used $\nabla_{\xi_{0,i}} \approx \nabla_{\xi_i}$ in the second step of the above equation. This is known as the Born approximation, and its validity on weak lensing power spectrum and GGL has been studied in, e.g. Hilbert et al. (2009).

The lensing convergence κ, shear (γ_1, γ_2), and rotation ω are related to the distortion matrix as

$$A = \begin{bmatrix} 1 - \kappa - \gamma_1 & -\gamma_2 - \omega \\ -\gamma_2 + \omega & 1 - \kappa + \gamma_1 \end{bmatrix}, \tag{18}$$

where one can relate the convergence κ to the density contrast $\delta \equiv \rho_m/\bar{\rho}_m - 1$, by using the Poisson equation:

$$\kappa = \frac{3}{2}\Omega_m H_0^2 \int_0^{\chi_s} g(\chi,\chi_s)\nabla^2\frac{\delta}{a}d\chi. \tag{19}$$

Using the Limber approximation, the convergence power spectrum can be written as

$$C_{\kappa\kappa}(\ell) = \int_0^{\chi_s} d\chi \frac{W(\chi)^2}{\chi^2}P_{\delta\delta}\left(k = \frac{\ell}{\chi}, z(\chi)\right), \tag{20}$$

where the lensing weight function $W(\chi)$ is given by

$$W(\chi) = \frac{3}{2}\Omega_m H_0^2 g(\chi,\chi_s)[1 + z(\chi)], \tag{21}$$

$P_{\delta\delta}$ is the matter power spectrum, and $z(\chi)$ is the redshift corresponding to comoving distance χ.

For GGL, we study the tangential shear profile around galaxies, which is given by

$$\gamma_t(r_p) = \frac{\Delta\Sigma(r_p)}{\Sigma_{crit}}, \tag{22}$$

where r_p is the projected distance from the galaxy, $\Delta\Sigma(r_p) \equiv \bar{\Sigma}(<r_p) - \Sigma(r_p)$ is the excess surface density defined as the

difference between the mean surface (projected) mass density at $r < r_p$, $\bar{\Sigma}(< r_p)$, and the surface mass density at r_p, $\Sigma(r_p)$:

$$\bar{\Sigma}(< r_p) = \frac{1}{\pi r_p^2} \int_0^{r_p} \Sigma(r) 2\pi r \, dr, \tag{23}$$

and Σ_{crit} is the critical surface mass density given as

$$\Sigma_{crit} \equiv \frac{1}{4\pi G} \frac{\chi_s}{\chi_l (\chi_s - \chi_l)} [1 + z(\chi_l)], \tag{24}$$

in which χ_l is the comoving distance of the lens galaxy. Note that, given that the background expansion history is in practice indistinguishable in the GR and F5 models studied here, Σ_{crit} is the same for both models.

For individual galaxies, the lensing signal is weak, and so we consider the stacking of the tangential shear profile around many galaxies. In practice, the excess surface density profile can be computed as

$$\Delta\Sigma(r_p) = \rho_{crit} \Omega_m \frac{2}{r_p^2} \int_{-\infty}^{\infty} d\chi \int_0^{r_p} dr \cdot r \xi_{gm} \left(\sqrt{r^2 + \chi^2} \right)$$
$$- \rho_{crit} \Omega_m \int_{-\infty}^{\infty} d\chi \, \xi_{gm}(r_p, \chi), \tag{25}$$

where ξ_{gm} is the cross-correlation function between galaxies and the matter density field.

2.3 Simulations and halo/galaxy catalogues

To accurately predict lensing effect in the non-linear regime requires numerical simulations of the matter distribution in the Universe. To cross-correlate this with galaxies requires mock galaxy catalogues with mimic the real galaxy distribution as observed by galaxy surveys. In this subsection, we shall describe in detail the simulations performed for this study, and halo and galaxy catalogues used in the analysis.

2.3.1 N-body simulations

The $f(R)$ gravity simulations used in our analysis have been run using the ECOSMOG code (Li et al. 2012), which is a modified version of the publicly available simulation code RAMSES (Teyssier 2002), by adding new modules to solve the $f(R)$ and Einstein equations. In this work, we have used the optimized version of the code (Bose et al. 2017), which adopts a new algorithm to speed up simulations for HS $f(R)$ model with $n = 1$ by a factor of up to ~20. RAMSES, and therefore ECOSMOG, is efficiently parallelized using MPI, and is an example of the class of so-called adaptive-mesh-refinement codes, which hierarchically refine a regular base mesh that covers the whole periodic simulation volume. In this way, it achieves the necessary high resolution in high-density regions, without wasting substantial amount of computing resources in low-density regions in which the demand for resolution is not as strong. The high resolution is also critical in order to resolve the fifth force effects in high-density regions, such as in dark matter haloes, where the chameleon screening makes them weak (but not always negligible).

The cosmological parameters, listed in Table 1, have been chosen from the best-fitting (WMAP Collaboration 2013) *WMAP9* ΛCDM model, and their physical meanings are explained in the table caption. The technical parameters for the simulations are given in Table 2. All simulations have 1024^3 particles.

Table 1. The cosmological parameters for the models investigated in this work. Ω_m and Ω_Λ are, respectively, the present-day fractional density of matter and the cosmological constant (in the case of $f(R)$ gravity, it is simply $1 - \Omega_m$). $h = H_0/(100 \, km \, s^{-1} \, Mpc^{-1})$ with H_0 being the present-day Hubble rate, n_s is the spectral index of the primordial density fluctuations, A_s the amplitude of the primordial power spectrum, and σ_8 the rms linear density fluctuation in spheres of radius $8 \, h^{-1} \, Mpc$ at $z = 0$ (the value quoted here is for ΛCDM model only, as F5 has a different value). Ω_b is the baryon density used for the linear matter power spectrum, to generate the initial conditions only.

Parameter	Physical meaning	Value
Ω_m	Present fractional matter density	0.2819
Ω_b	Present fractional baryon density	0.0461
Ω_Λ	$1 - \Omega_m$	0.7181
h	$H_0/(100 \, km \, s^{-1} \, Mpc^{-1})$	0.6970
n_s	Primordial power spectral index	0.9710
$\log_{10} A_s$	Amplitude of the primordial power spectrum	-8.622
σ_8	Rms density fluctuation at $8 \, h^{-1} \, Mpc$ for ΛCDM	0.8178
n	HS $f(R)$ parameter	1.0
f_{R0}	HS $f(R)$ parameter	-10^{-5}

Table 2. The simulation specifications. L_{box} is the simulation box size, N_p is the number of simulation particles, m_p the simulation particle mass, N_r the number of realizations for each box size, and N_s the number of particle outputs (which are spaced every $75 \, h^{-1} \, Mpc$ in comoving distance from today). z_{ini} is the starting redshift of the simulations, and the initial condition is generated using the 2LPTIC code. Out of the N_s snapshots, 33 are between $z = [0, 1]$.

L_{box} (h^{-1} Mpc)	z_{ini}	N_p	m_p ($h^{-1} M_\odot$)	N_r	N_s	IC
450	49.0	1024^3	6.64×10^9	1	37	2LPT
900	36.0	1024^3	5.31×10^{10}	1	37	2LPT

The initial conditions of the simulations are generated using the 2LPTIC code which is based on second-order Lagrangian perturbation theory (Crocce, Pueblas & Scoccimarro 2006). Since we keep the simulation particle number N_p fixed to be 1024^3, for our larger boxes the mass resolution is relatively low, and so following Shirasaki, Hamana & Yoshida (2015) we compensate this by starting those simulations at relatively low redshifts. For each F5 simulation, we run a ΛCDM simulation with exactly the same cosmological parameters and simulation specifications for comparison; the ΛCDM simulations also start from the same initial conditions as their F5 counterparts, because at $z_{ini} \gg 1$ the difference between the two models is negligible. We only have one realization of simulation for each box size.

2.3.2 Halo and galaxy catalogues

The dark matter haloes used in this paper are found using the publicly available phase-space friend-of-friend halo finder ROCKSTAR (Behroozi, Wechsler & Wu 2013), and we have chosen M_{200c} as the mass definition, in which the subscript means that the average mass density within halo radius R_{200c} is 200 times the critical density ρ_c.

We populate dark matter haloes using HOD (Berlind et al. 2003; Zheng et al. 2005). In the simplest form of this model, the mean number density of galaxies in a host dark matter halo is a function of the halo mass M:

$$\langle N_g | M \rangle = \langle N_c | M \rangle [1 + \langle N_s | M \rangle], \tag{26}$$

where N_g, N_c, and N_s are, respectively, the number of all, central, and satellite galaxies, given as

$$\langle N_c | M \rangle = \frac{1}{2} \left[1 + \mathrm{erf} \left(\frac{\log M - \log M_{\min}}{\sigma_{\log M}} \right) \right], \qquad (27)$$

$$\langle N_s | M \rangle = \left(\frac{M - M_0}{M_1} \right)^{\alpha} \Theta \left(M - M_0 \right), \qquad (28)$$

where $\mathrm{erf}(x)$ and $\Theta(x)$ are, respectively, the error and Heaverside step functions. The model has five parameters: $M_{\min}, M_0, M_1, \sigma_{\log M}$, and α, which give it great freedom to tune the galaxy catalogues to match their statistical properties to observables.

To implement the HOD model, we shift through the halo catalogue where subhaloes are eliminated, and for each halo let it host a central galaxy if $u \leq \langle N_c | M \rangle$ where u is a random number generated from a uniform distribution between [0, 1]. The number of satellite galaxies is set to a random number generated from the Poisson distribution with mean $\langle N_s \rangle$, and the satellite galaxies are radially distributed within the dark matter halo following the Navarro–Frenk–White (Navarro, Frenk & White 1997) profile, using the concentration parameters measured by ROCKSTAR. In the rare cases where a halo has no central galaxy but does have satellites, we promote the first satellite galaxy to a central galaxy.

Although this paper does not aim to compare theoretical predictions with real observations, we still want the HOD catalogues to bear a certain degree of reality. To this end, we focus on galaxies at relatively low redshift (where the model difference is expected to be larger) and make the resulting galaxies satisfy a redshift distribution similar to that of the low-redshift sample (LOWZ) of Baryon Oscillation Spectroscopic Survey (BOSS) data release 11. Instead of downsampling generated HOD catalogues, we follow Manera et al. (2015) to allow a redshift dependence of the HOD mass parameters as follows:

$$\log M_{\min} = \log M_{\min}^{*} + Sn(z)/\left(10^{-4} \right), \qquad (29)$$

$$\log M_{0,1} = \log M_{0,1}^{*} + Tn(z)/\left(10^{-4} \right), \qquad (30)$$

in which $n(z)$ is the target galaxy number density for redshift z, $S = -0.925$, $T = -0.928$, and M^{*} are the respective mass parameter values at $n^{*} = 2.98 \times 10^{-4}$. Note that M_1/M_0 has no time evolution. We consider galaxies in the redshift range of $0.16 \lesssim z \lesssim 0.43$. We use 29 redshift bins in this range, with equal comoving thickness, with three bins being taken from each of the 10 snapshots of this box. For the three bins from the same simulation snapshot, the evolution of $n(z)$ is only down to equations (29) and (30), while for the bins from different snapshots $n(z)$ is also affected by the fact that different halo catalogues have been used to build the HOD catalogues.

Should the HOD catalogues in F5 have been constructed with the same HOD parameters as in their ΛCDM counterparts, there would generally be a difference of $\sim$10 per cent–20 per cent in the number density and clustering of galaxies. Because there is only one observed galaxy catalogue in the Universe (assuming an ideal full-sky survey), if we do not know which is the correct cosmological model, we can only demand that both models make predictions that agree with observations. For this reason, we have opted to tune the HOD parameters for F5 so that the resulting galaxy catalogues match the number density and clustering of their ΛCDM counterparts. The assumption that F5 and GR should have different HOD parameters is not unreasonable, given their different dark matter evolutions and

galaxy assembly histories. This choice indeed also helps to fix the galaxy clustering and single out the expected difference of the GGL signals in these two models.

The tuning of F5 HOD parameters has been performed using a search with the Nelder–Mead simplex algorithm through the 5D parameter space. The 3D real-space correlation functions in the F5 and GR HOD catalogues are measured between comoving separations of 0.6 and $60 \, h^{-1}$ Mpc, in 40 equally spaced logarithmic bins. The root-mean-squared (rms) difference between the two models is calculated with equal weight 1 for all bins. To try to make the two models have similar $n(z)$, the relative difference in their $n(z)$ values is also added into the rms, with a weight 8. The code then searches through the 5D parameter space looking for the smallest rms difference (χ^2). The search stops when $\chi^2 < 0.03$, meaning that the overall agreement (as defined in the above way) is better than 3 per cent (for some redshift bins better than 2 per cent). We have not attempted to do better than this accuracy, or perform a full parameter search using Markov chain Monte Carlo, because it is not the purpose of this paper to study in great detail the HOD model in the context of MG, and because it is in general difficult to do better than this level of accuracy (for example, the galaxy clustering may change at few per cent level if a different set of random seeds is used in generating the HOD catalogues). For the same reason, we shall not list the HOD parameters in this paper.

In the left-hand panel of Fig. 1, we compare the measured 3D real-space correlation functions $\xi(r)$ as a function of galaxy separation r, respectively for F5 (red dashed lines) and GR (blue solid) at 6 of the 29 redshift bins. In the right-hand panel of Fig. 1 (the same colour scheme) shows the redshift distribution of the HOD galaxies for the two models – again there is a good agreement (generally better than 4 per cent) after tuning the HOD parameters for F5.

3 WEAK GRAVITATIONAL LENSING IN F(R) GRAVITY

In this section, we present the main result of this research, beginning with an analysis of the weak lensing convergence. The convergence power spectrum in $f(R)$ gravity, amongst various other things, have been studied in a few works (Shirasaki et al. 2015, 2017; Higuchi & Shirasaki 2016; Tessore et al. 2015; Pratten et al. 2016), using various techniques. We revisit this topic in Section 3.1 with a detailed decomposition of the convergence power spectrum $C_{\kappa\kappa}(\ell)$ in terms of the length-scales and times where the contributions to the relative difference between $f(R)$ gravity and GR come from. The analysis not only serves as a sanity check of the simulations and their corresponding particle snapshots, but also will be used for comparison with results on GGL from Section 3.2, as they are based on the same set of simulations.

3.1 The convergence field

The weak lensing convergence is an important physical quantity for weak lensing research: it can be calculated directly from a simulation by a projection of the density field, and in the regime of weak lensing its power spectrum coincides with that of the cosmic shear, which is a directly observable quantity. It has been one of the most widely used quantities in theoretical analyses (see reference above for examples in $f(R)$ gravity).

3.1.1 The convergence power spectrum in f(R) gravity

In this work, we compute the weak lensing convergence power spectrum $C_{\kappa\kappa}(\ell)$ by directly integrating the 3D matter power
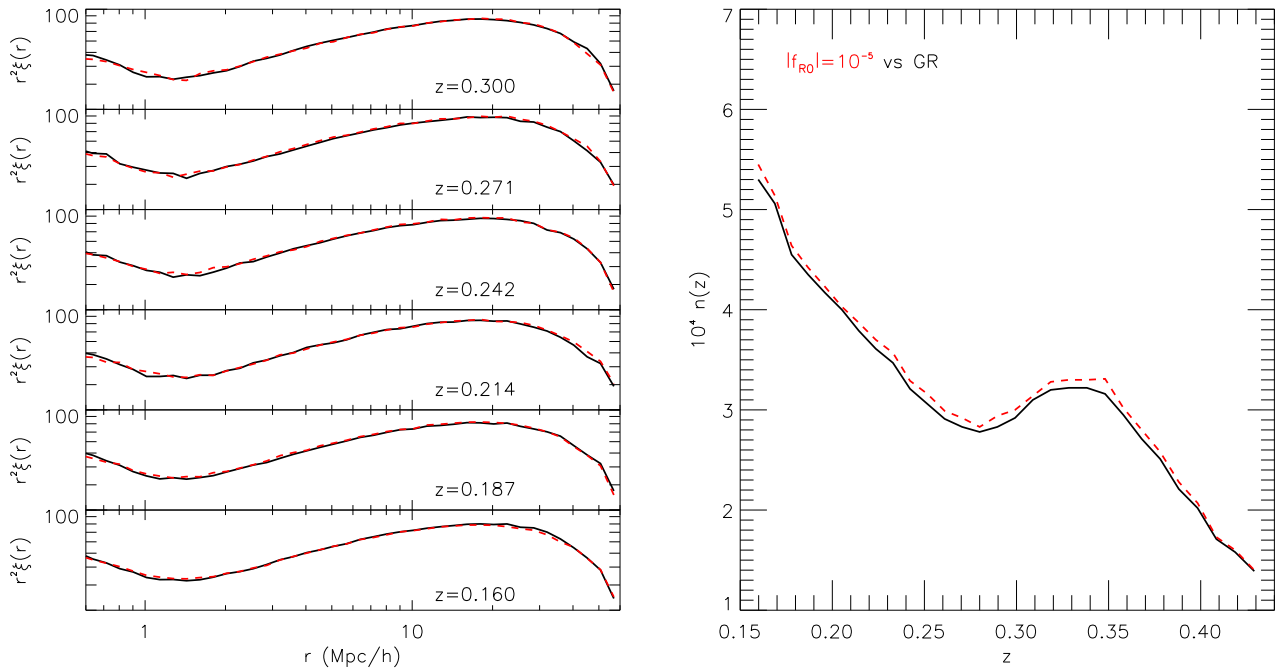
Figure 1. Left-hand panels: comparison of the GR (black solid) and F5 (red dashed) correlation functions, after tuning the HOD parameters for F5 such that the two models predict similar galaxy number densities and clusterings. For clearness, we only show results for 6 of the 29 redshift bins from the $900\,h^{-1}$ Mpc box. Each bin is taken from HOD catalogues built using a different output snapshot. Right-hand panel: comparison of the predicted GR (black solid) and F5 (red dashed) galaxy redshift distributions. See the text for more details on how the galaxy numbers in each redshift bin are determined for GR and F5.

spectrum $P_{\delta\delta}(k, z)$ measured from the simulations, following the Limber approximation equation (20), instead of using full ray tracing. This is partly because the former approach essentially samples all the relevant k modes provided by the simulation, while ray tracing only samples those k modes that fall into the designed light-cone. While the latter more closely mimics the real Universe, the former gives smoother theoretical curves equation (20), together with an accurate prediction of the non-linear $P_{\delta\delta}$ such as from HALOFIT (Smith et al. 2003; Takahashi et al. 2012), is a powerful tool to predict $C_{\kappa\kappa}$.

The non-linear $P_{\delta\delta}$ used in this work are measured using the publicly available POWMES code (Colombi & Novikov 2011) with a fast Fourier transform grid of size 2048^3. As mentioned above, our simulations have outputs at 33 snapshots between $z = 1$ and 0 equally spaced in comoving distance ($\Delta\chi = 75\,h^{-1}$ Mpc), and therefore this is the finest grid in z (or in χ) that our integration of equation (20) can be carried out. We used the five-point Newton–Cotes formula for the numerical integration over χ, and values of $P_{\delta\delta}(k)$ at a given redshift $z(\chi)$ were obtained by linear interpolation of the corresponding values at k_i, k_{i+1} with $k_i < k < k_{i+1}$, where k_i is the ith grid point in the POWMES output. To check that such a coarse spacing in χ is not causing substantial numerical errors, we made a test using a finer sampling of $P_{\delta\delta}(k, z(\chi))$ in the χ direction, with a comoving thickness of $25\,h^{-1}$ Mpc, generated using HALOFIT. We then integrated this sample (1) using all χ bins, and (2) using one from every three neighbouring bins (the latter mimicking the simulation binning of $\Delta\chi = 75\,h^{-1}$ Mpc). The results of these two tests are shown as black and blue solid lines in the upper left panel of Fig. 2, and their relative difference is presented as the blue solid line in the lower left panel. The tests showed that the difference is much smaller than 1 per cent, and that $\Delta\chi = 75\,h^{-1}$ Mpc is fine enough for our study. We have also checked that the convergence power spectrum (for GR) computed in this way agreed well with the result

of CAMB (Lewis & Challinor 2011) for the same cosmology, though note that to match the k range of the simulated $P_{\delta\delta}(k, z)$ we have limited the maximum k in the integration to $k_{max} = 28.6\,h\,\mathrm{Mpc}^{-1}$, which affects $C_{\kappa\kappa}$ a little bit at $\ell \sim 10^4$.

The red solid line in the upper left panel of Fig. 2 is the result of the same integration of the simulated $P_{\delta\delta}(k, z)$ for GR, and the red solid line in the lower left panel is the relative difference from the integration of HALOFIT $P_{\delta\delta}(k, z)$. The simulation result peels off at $\ell \lesssim 20$ because the lowest k values used in the integration is $k_{min} \sim 0.014\,h\,\mathrm{Mpc}^{-1}$, and the same feature appeared in the HALOFIT results if the same k_{min} was applied there. We notice that the simulation and HALOFIT results agree reasonably well, with the former lower by $\sim$2 per cent in a wide range of ℓ, possibly due to sampling variance (recall that the simulation box is $450\,h^{-1}$ Mpc). The difference between the two further changes to 5 per cent−6 per cent when ℓ approaches 10^4, due to slight loss of resolution by the simulation.

The right-hand panels of Fig. 2 compare the convergence power spectra of F5 (red) and GR (black), for two lensing source redshifts, $z_{source} = 1.0$ (solid) and $z_{source} = 0.5$ (dashed). For both source redshifts, an enhancement of order 10 per cent−30 per cent between $\ell \sim 100$ and 10^4 is found, which increases with ℓ, and the relative difference is larger in the case of $z_{source} = 0.5$.

3.1.2 The connection between matter and convergence spectra

To gain a clearer understanding of the behaviour shown in the right-hand panels of Fig. 2, recall from equation (20) that $C_{\kappa\kappa}(\ell)$ at a given angular scale ℓ gets contribution from various k modes of the non-linear $P_{\delta\delta}$ from different times. It is therefore useful to decompose the contributions from the different times and k modes, on to which we can readily map the relative differences in $P_{\delta\delta}(k, z)$ themselves. Fig. 3 shows the results from such an attempt for $z_{source} = 1$ (left-hand panel) and $z_{source} = 0.5$ (right-hand panel).

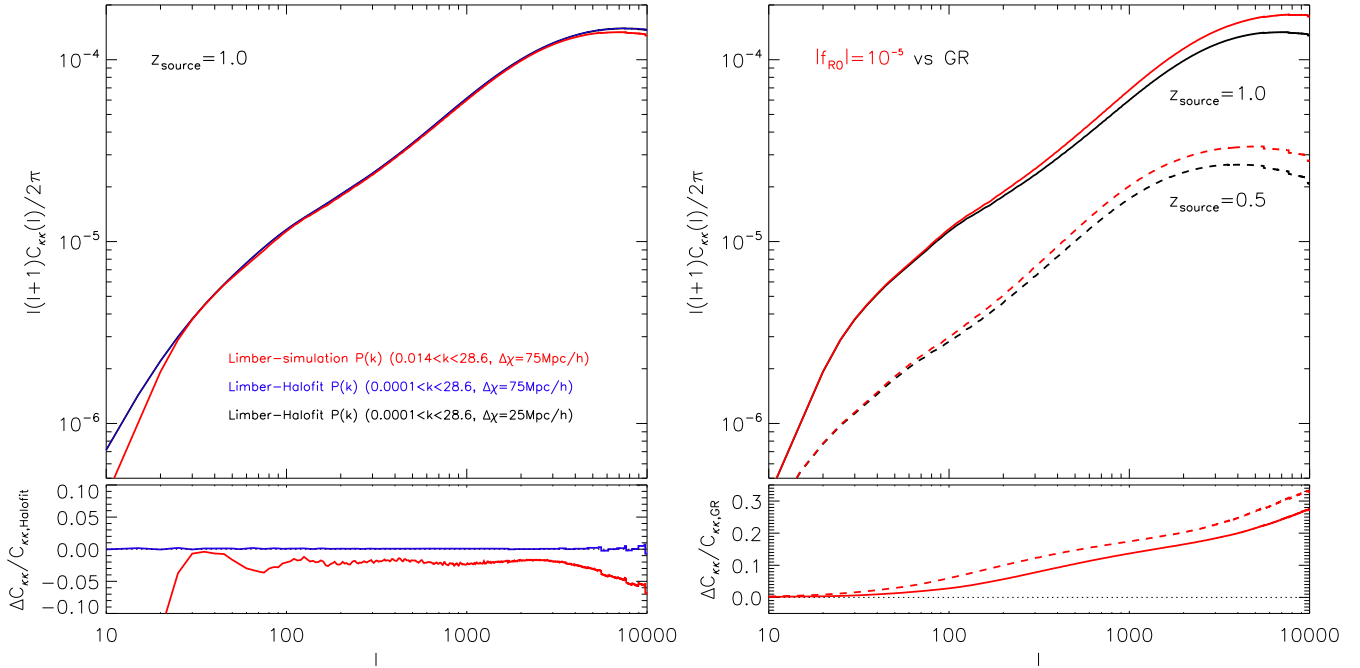**Figure 2.** Left-hand panels: the effect of choosing a coarser – $\Delta\chi = 75\,h^{-1}$ Mpc in blue solid versus $\Delta\chi = 25\,h^{-1}$ Mpc in black solid – sampling of $P(k, z)$ (generated using HALOFIT) when using the Limber approximation equation (20) to compute the convergence power spectrum $C_{\kappa\kappa}(\ell)$. The solid red line shows the result of doing the same integration with $\Delta\chi = 75\,h^{-1}$ Mpc, but for the simulated $P(k, z)$. The lower subpanel shows the relative differences of the other two cases with respect to the integration of HALOFIT $P(k, z)$ with $\Delta\chi = 25\,h^{-1}$ Mpc. Right-hand panels: the convergence power spectra for F5 (red) and GR (black), using two source redshifts $z_{\text{source}} = 1.0$ (solid) and 0.5 (dashed) – all results are from integrating the simulated $P(k, z)$ following equation (20). The lower subpanel shows the relative differences between F5 and GR. See the main text for discussions of this plot.
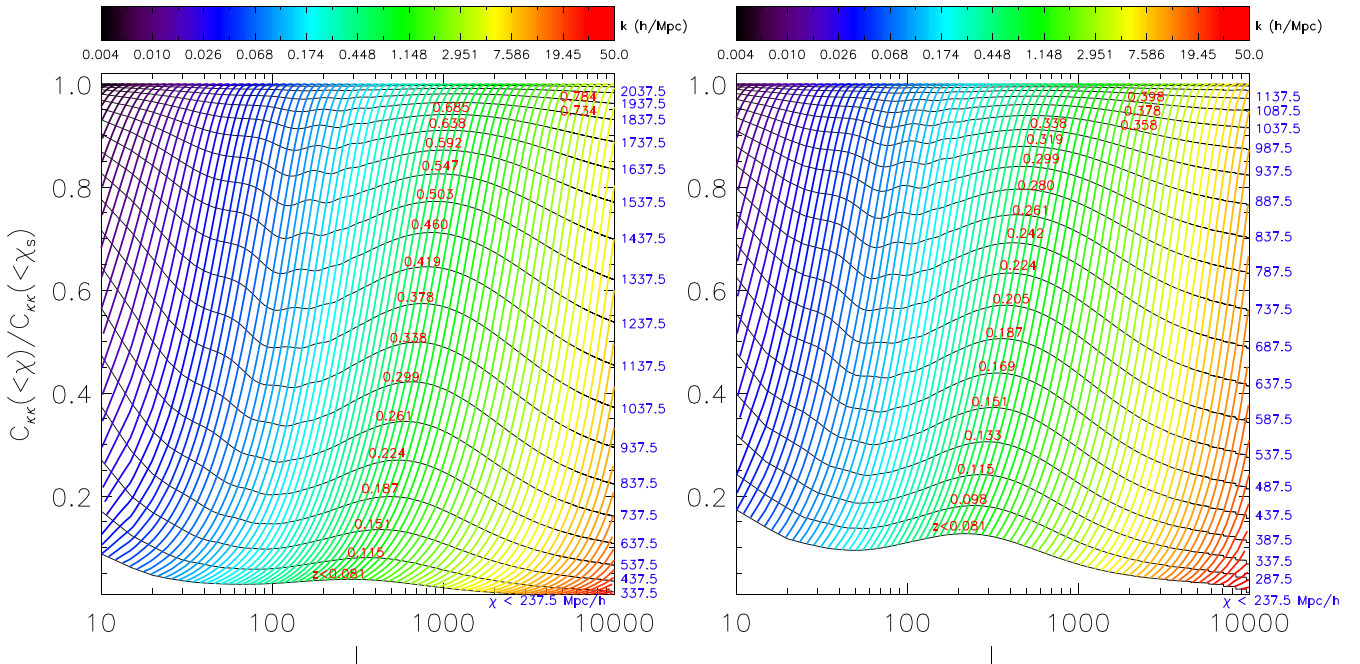
Figure 3. A detailed decomposition showing how much the different time (redshift) intervals and k modes in the non-linear matter power spectrum $P_{\delta\delta}(k, z)$ contribute to the convergence power spectrum $C_{\kappa\kappa}(\ell)$ at a given ℓ. The decomposition is done for two source redshifts: $z_{\text{source}} = 1.0$ (left-hand panel) and 0.5 (right-hand panel). The vertical axis is the fractional contribution from distances smaller than a given χ, defined as $C_{\kappa\kappa}(<\chi)/C_{\kappa\kappa}(<\chi_{\text{s}})$, and the black solid lines are the values for a selection of χ values (indicated in blue; the corresponding redshift values are indicated in red) in step of $100\,h^{-1}$ Mpc (for $z_{\text{source}} = 1$) and $50\,h^{-1}$ Mpc (for $z_{\text{source}} = 0.5$). The colour-coded solid lines (roughly) in the vertical direction are curves with constant k values that contribute to a given ℓ at a given time z (or χ), with $k = \ell/r(\chi)$. The value of k for each of these curves can be found using the colour bar on the top, which runs from black ($k = 0.004\,h\,\text{Mpc}^{-1}$) to red ($k = 50\,h\,\text{Mpc}^{-1}$). Note that each ℓ in $C_{\kappa\kappa}(\ell)$ receives contributions from a limited range of k (which shifts to larger values for decreasing z_{source}), and that most contributions are from low and middle redshifts.
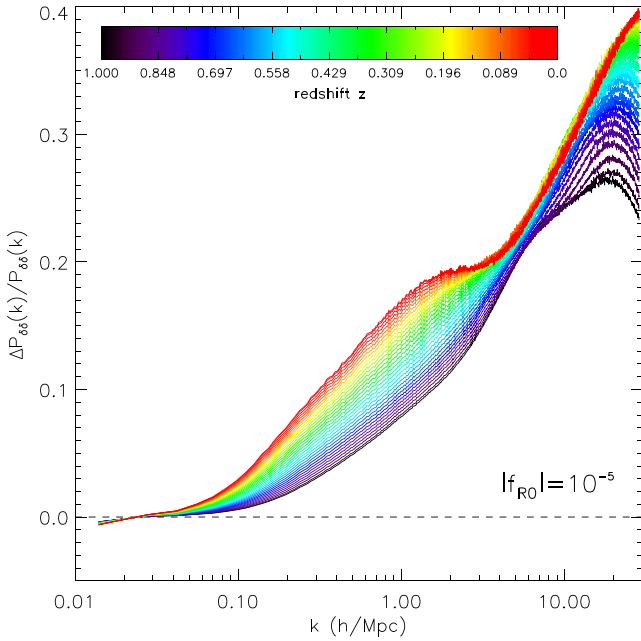
Figure 4. The relative enhancement of the non-linear matter power spectrum $P_{\delta\delta}$ in F5 relative to GR, as a function of k (the horizontal axis) and redshift $z(\chi)$ (equally spaced in χ with a $\Delta\chi = 75\,h^{-1}\,\mathrm{Mpc}$; colour-coded according to the colour bar on the top).

In both cases, the plot is the fractional contribution (black solid curves) from distances below a specific χ (indicated with the blue numbers to the right of the right axis; in units of $h^{-1}\,\mathrm{Mpc}$) against ℓ. On the top of each black solid curve, the red number indicates the redshift of the corresponding χ. The colour-coded lines along the vertical direction denote the values of k that contributes at the given ℓ (as shown in the horizontal axis) and χ (as represented by the black solid curves); each of them corresponds to a fixed k with the colour scheme as displayed in the colour bar on the top (running from black for $k \sim 0.004\,h\,\mathrm{Mpc}^{-1}$ to red for $k = 50\,h\,\mathrm{Mpc}^{-1}$). From Fig. 3, we see the well-known result that most contributions at large (small) angular scales come from large (small) length scales; it also indicates that most contributions come from middle and low redshifts – for example, $\sim$90 per cent contributions in the case of $z_{\mathrm{source}} = 1$ (0.5) come from the redshift range $z \lesssim 0.7$ ($z \lesssim 0.38$).

Fig. 4 shows how the relative difference in the non-linear $P_{\delta\delta}$ of F5 and GR evolves in time. We can see the known feature (e.g. Li et al. 2013) that the F5 prediction agrees with GR on large scales due to the finite ranges of the modified gravitational force, and the enhancement of clustering on non-linear scales ($k \geq 0.1\,h\,\mathrm{Mpc}^{-1}$). We show 33 curves corresponding to the 33 snapshots between $z = 1$ (black) and $z = 0$ (red), which give us a comprehensive picture of not only the k but also the time dependencies of the enhancement. For examples:

(i) At $k \sim 0.1\,h\,\mathrm{Mpc}^{-1}$, the relative enhancement of $P_{\delta\delta}$ for F5 is within 1 per cent$-$3 per cent between $z = 1$ and 0. According to Fig. 3, this k mode is most relevant for $\ell \sim 100$, which explains the $\sim$2 per cent enhancement of $C_{\kappa\kappa}$ there (cf. Fig. 2, the $z_{\mathrm{source}} = 1$ case – the same below).

(ii) At $k \sim 1\,h\,\mathrm{Mpc}^{-1}$, $P_{\delta\delta}$ in F5 is enhanced by 10 per cent$-$18 per cent between $z \sim 0.7$ and $z = 0$, leading to a $\sim$15 per cent of $C_{\kappa\kappa}$ at $\ell \sim 1000$.

(iii) Between $k = 1$ and a few $h\,\mathrm{Mpc}^{-1}$ is the transition regime between one- and two-halo terms in the halo model, where the

enhancement in F5 $P_{\delta\delta}$ increases more slowly with k than at lower k values. This is reflected as a slight flattening of $\Delta C_{\kappa\kappa}/C_{\kappa\kappa}$ at ℓ just above 1000 (Fig. 2).

(iv) At $k \sim 5\,h\,\mathrm{Mpc}^{-1}$, the relative enhancement of F5 $P_{\delta\delta}$ remains nearly a constant at $\sim$20 per cent within $z = 1$ and 0, which translates into a $\sim$20 per cent enhancement of F5 $C_{\kappa\kappa}$ at $\ell \sim 4000$–5000 (Fig. 2).

(v) At $k > 5\,h\,\mathrm{Mpc}^{-1}$, there is another steep increase of the enhancement in F5 $P_{\delta\delta}$ with k, indicating that dark matter haloes (at least the small ones which dominate in number) in F5 are more concentrated. This further increases $\Delta C_{\kappa\kappa}/C_{\kappa\kappa}$ above $\ell \sim 4000$–5000.

(vi) At all ℓ, $\Delta C_{\kappa\kappa}/C_{\kappa\kappa}$ is larger in the case of $z_{\mathrm{source}} = 0.5$ than for $z_{\mathrm{source}} = 1.0$, because in the former case the result is dominated by lower redshifts in the integration equation (20), at which the enhancement of the non-linear matter power spectrum in F5 relative to in GR is stronger.

The results here agree with those found in Tessore et al. (2015) and Shirasaki et al. (2017), and so serve as a sanity check of the simulations. Moreover, the decomposition of Fig. 3 provides a way to qualitatively understand the behaviour of the convergence power spectra based on knowledge about the scale and time dependencies of the non-linear matter power spectra. It can also prove useful when decomposing the degeneracies of MG with other physical effects that can modify $P_{\delta\delta}$ on intermediate and small scales, such as active galactic nuclei feedback and massive neutrinos (see Semboloni et al. 2011; Osato, Shirasaki & Yaoshida 2015; Mummery et al. 2017, for some general examples) (and see also e.g. Arnold, Puchwein & Springel 2014; Harnois-Deraps et al. 2015, for some examples in the framework of MG).

3.2 Galaxy–galaxy weak lensing

Having looked at the behaviour of the lensing power spectra, now we move to the theoretical predictions of galaxy–galaxy weak lensing.

3.2.1 The galaxy–matter cross-correlation

The correlation of shearing of source galaxies behind lens galaxies is given by the tangential shear profile around the lenses, which in turn is related to the excess surface density profile $\Delta\Sigma(r_{\mathrm{p}})$. This can be calculated by integrating $\xi_{\mathrm{gm}}(r)$ along the los, and means that information about ξ_{gm} can be obtained by studying GGL. For this reason in this subsubsection, we shall compare the theoretical predictions of ξ_{gm} by GR and F5.

We measure ξ_{gm} directly by cross-correlating the mock galaxy catalogues with the particle data from which they (and the corresponding halo catalogues) are constructed. This is done by a modified version of the publicly available CUTE_BOX code (Alonso 2012). We have not downsampled the dark matter particles, and for a galaxy number of $N_{\mathrm{g}} \sim 3 \times 10^5$ and dark matter particle number $N_{\mathrm{p}} = 1024^3$ the code generally finishes for a snapshot in a few hours using 12 threads. For the autocorrelation function of matter, ξ_{mm}, the cost is prohibitive without downsampling particles, and we instead calculate it by directly transforming the matter power spectra $P_{\delta\delta}$ (see below).

In order to estimate the uncertainties caused by the larger scale environment, we use the internal jackknife resampling method with N_{JK}^3 resamples by dividing the simulation box into N_{JK}^3 sub-boxes of equal volume. For each resample, we discard the galaxies in one of the sub-boxes, but still include matter from that sub-box when cross-correlating with galaxies in other sub-boxes. The cross-correlation
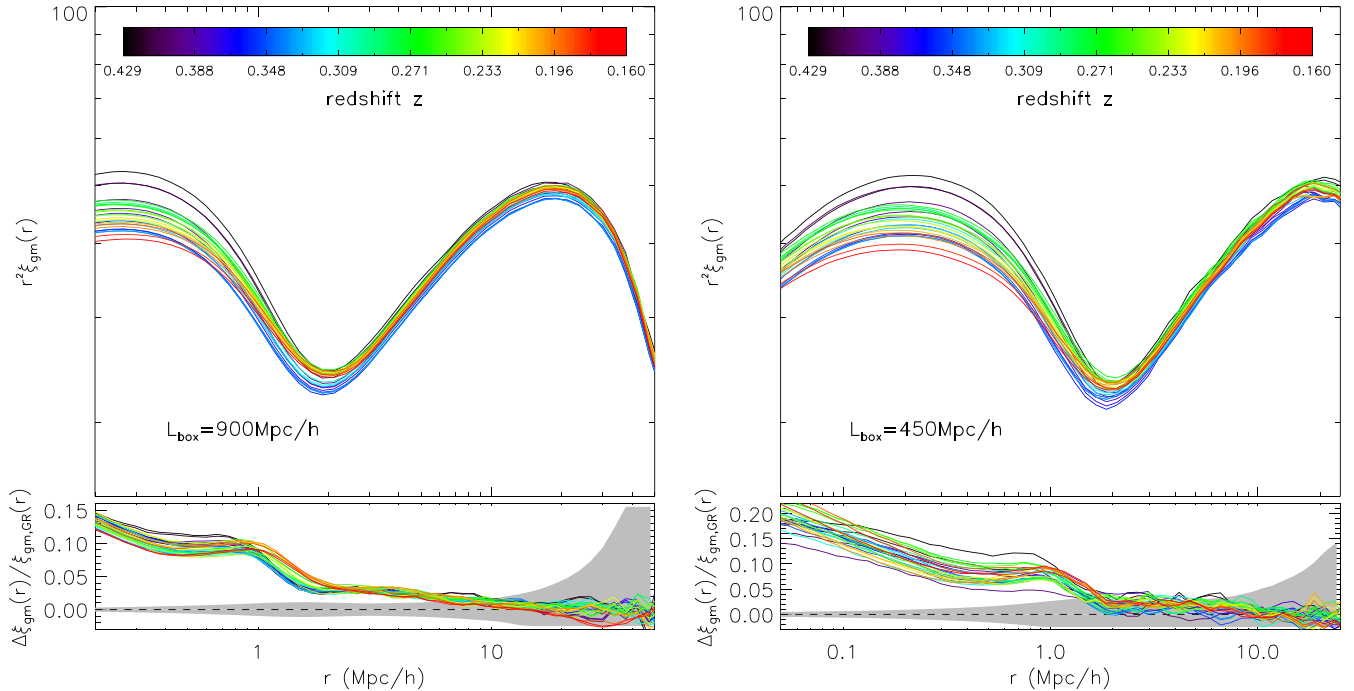
Figure 5. Top left panel: the galaxy–matter cross-correlation function $\xi_{gm}(r)$, as a function of the separation r of the galaxy–particle pair, for the 29 of HOD galaxy catalogues constructed using the GR $L_{box} = 900\,h^{-1}$ Mpc simulation. The colours of the curves indicate the redshift z (see the colour bar on the top). To clarify, we have shown $r^2\xi_{gm}(r)$ and have not plotted the curves for F5. Bottom left panel: the relative differences between the F5 and GR predictions of ξ_{rm} for the 29 HOD catalogues, using the same colour scheme. The grey shaded region marks the 1σ error from the 125 Jackknife resamples. Right-hand panels: the same but for the simulation with $L_{box} = 450\,h^{-1}$ Mpc.

function of the ith jackknife resample, $\xi_{gm}^{(i)}$, is estimated as

$$1 + \xi_{gm}^{(i)}(r, r + \Delta r) \equiv \frac{N_{DD}^{(\bar{i})}(r, r + \Delta r)}{N_p N_g^{(\bar{i})} \Delta V / V} = \frac{N_{DD}^{(\bar{i})}(r, r + \Delta r)}{n_p N_g^{(\bar{i})} \Delta V}, \quad (31)$$

where V is the whole volume of the simulation box, ΔV is the volume of the radius bin $[r, r + \Delta r]$, N_p the total number of dark matter particles in the simulation volume, $n_p = N_p/V$, and $N_g^{(\bar{i})}$ the number of galaxies and $N_{DD}^{(\bar{i})}(r, r + \Delta r)$ the number of galaxy–particle pairs in radius bin $[r, r + \Delta r]$ when the ith jackknife sub-box is excluded. Note that we only discard the galaxies (and not the dark matter particles) in the ith jackknife sub-box when counting the pairs. We use $N_{JK} = 5$ in this work. Note that the jackknife error estimates do not include shape noises of source galaxies and the noises due to finite number of sources. Also, by directly integrating the galaxy–matter cross-correlation function ξ_{gm}, we essentially perform the integration along all possible lines of sight and so the statistical error is smaller than that obtained using a sample of the same volume and number density of lens objects in real observations, where one has only a single los for each object. For a more detailed analysis of errors using mock lensing data, see Shirasaki et al. (2016).

Fig. 5 presents the galaxy–matter cross-correlation functions measured from the $L_{box} = 900$ (left) and $450\,h^{-1}$ Mpc (right) simulations, and for each case we show, in the top panel, the GR results for all 29 snapshots of HOD catalogues (the coloured solid curves, with the colours denoting the redshifts according to the colour bar). In the lower panels, we show the relative differences between F5 and GR using the same redshift–colour scheme, and the grey shaded region marks the 1σ Jackknife error. Notice that to improve visibility, we have plotted $r^2\xi_{gm}(r)$ instead of $\xi_{gm}(r)$ itself in the top panels. The results from the two boxes agree with each other well.

The GR curves in Fig. 5 show a scatter of up to $\sim$10 per cent, which is because the different HOD catalogues do not correspond to the same set of tracers of the density field. To see this more explicitly, let us remark that the galaxy number density in our HOD catalogues peaks at $z \sim 0.16$, and as we go to higher redshifts it first decreases until $z \sim 0.27$, when it begins to increase, and then from $z \sim 0.33$ it starts to decrease again. The same trend can be seen in the ξ_{gm} curves of Fig. 5, namely the curves become higher from $z \sim 0.16$ (red) to 0.27 (green), then lower between $z \sim 0.27$ and 0.33 (blue), and then higher again until $z \sim 0.43$ (black). The trend is the same from both boxes. Physically, according to our HOD model, a lower galaxy number density indicates that only the more massive haloes are populated with galaxies, and these haloes have stronger correlations with matter around and inside. The behaviour is hence not surprising: when we consider the cross-correlation between the matter density field and its tracers, the choice of the latter is critical (we will revisit this point later).

What is more interesting is the relative difference between F5 and GR, which is shown in the lower panels of Fig. 5. There we see that the two models agree with each other (within the Jackknife error) at $r > 10\,h^{-1}$ Mpc, that F5 ξ_{gm} starts to get enhanced – with a modest enhancement factor of 3 per cent–5 per cent – relative to the GR result at $r < 10\,h^{-1}$ Mpc, and finally near the transition scale between one- and two-halo terms ($r \sim 1$–$2\,h^{-1}$ Mpc) the enhancement factor increases to $\sim$10 per cent. The stronger enhancement in the regime where the one-halo term dominates is related to the more concentrated matter distribution in F5 compared to GR. Note that the model difference, unlike the cross-correlation function ξ_{gm} itself, is less dependent on redshift and therefore less sensitive to the choice of tracers. This is also as expected, because the selection of tracers in our HOD modelling affects both models in a similar way.
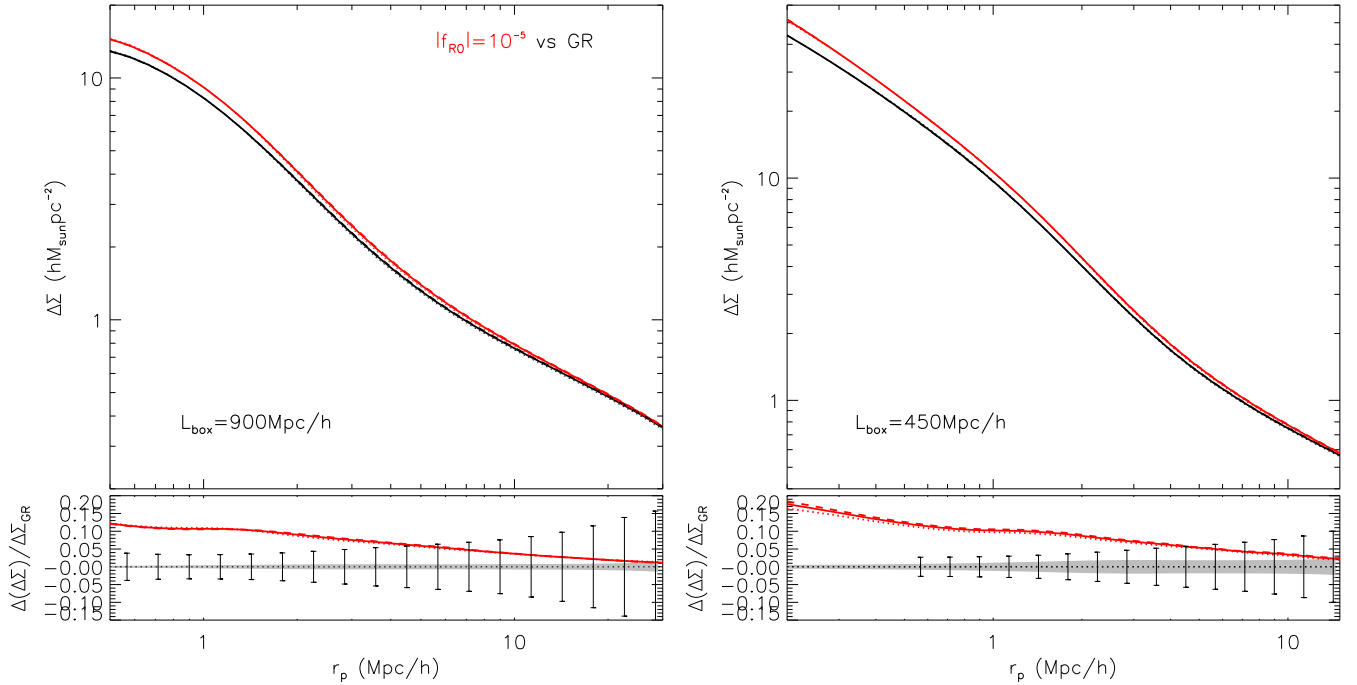
Figure 6. Top left panel: the excess surface density profiles as functions of the projected separation r_p, measure from the $L_{box} = 900\,h^{-1}$ Mpc GR (black solid line) and F5 (red solid line) simulations, assuming a stack around all galaxies in the 29 snapshots of HOD galaxies. The dotted and dashed lines – with the same colour – are the results of using the 14 high-redshift ($0.30 \lesssim z \lesssim 0.43$) and 15 low-redshift ($0.16 \lesssim z \lesssim 0.29$) HOD catalogues, and they are barely visible in the plot. Bottom left panel: the relative difference between F5 and GR, using the same line styles and colours (now the difference between the high-z and low-z galaxy samples is clearer but still very small). The grey shaded region shows the square root of the diagonal elements of the Jackknife covariance matrix, and the error bars are the square root of the diagonal elements of the analytical covariance matrix assuming the HSC survey. Right-hand panels: the same but for the simulation with $L_{box} = 450\,h^{-1}$ Mpc.

3.2.2 The excess surface density profiles

The averaged excess surface density profile, $\Delta\Sigma(r_p)$, is calculated by directly integrating the galaxy–mass cross-correlation functions, following the prescription of equation (25).

To calculate this, we first use cubic spline to interpolate the $\xi_{gm}(r = \sqrt{r_p^2 + z^2})$ measured from the simulations on to a grid in $(\log(r_p), z)$, where r_p is the projected separation and z is the los coordinate (with $z = 0$ at the position of the galaxy),[4] and then perform the integrations using direction summation. We have chosen a fine interpolation grid, as well as a large enough z_{max} for the los integration, so that the percentage error for the numerical integrations is within ~ 0.1 per cent. For the $L_{box} = 900\,h^{-1}$ Mpc ($450\,h^{-1}$ Mpc) simulations, this allows us to have $\Delta\Sigma(r_p)$ up to $r_p = 30\,h^{-1}$ Mpc ($15\,h^{-1}$ Mpc), with $z_{max} = 90\,h^{-1}$ Mpc ($\sim 65\,h^{-1}$ Mpc).

The left-hand (right-hand) panel of Fig. 6 shows the results of $\Delta\Sigma(r_p)$ from the $L_{box} = 900(450)\,h^{-1}$ Mpc simulation. A comparison of the upper panels indicates that the $900\,h^{-1}$ Mpc box starts to lose resolution at $r_p \sim 1\,h^{-1}$ Mpc, but the relative difference between F5 and GR agrees down to $r_p \sim 0.5\,h^{-1}$ Mpc. In both cases, we have split the lens galaxies into two separate redshift ranges (a high-z bin with $0.30 \lesssim z \lesssim 0.43$ and a low-z bin with $0.16 \lesssim z \lesssim 0.29$), but the results – dotted and dashed lines, respectively – display barely any difference from using the whole lens galaxy sample, suggesting that the conclusion does not depend sensitively

on redshift or the source number density, at least in the redshift range covered in this study.

The stacked excess surface density profiles in F5 and GR differ most significantly at $r_p \lesssim 2\,h^{-1}$ Mpc, which reflects the bigger difference in the one-halo term of the matter–galaxy correlation function as shown in Fig. 5. The model difference between F5 and GR has a distinct dependence on r_p from that of $\xi_{gm}(r)$, which is ~ 5 per cent–10 per cent at $1 \lesssim r_p \lesssim 10\,h^{-1}$ Mpc, because $\Delta\Sigma(r_p)$ depends on the average ξ_{gm} from $R = 0$ to r_p, where R is the projected distance from the lens. Although this means that one can see a strong signal up to larger values of r_p, it also implies that uncertainties that affect the prediction of the one-halo term in ξ_{gm}, such as baryonic physics, can have an impact on $\Delta\Sigma$ to larger r_p, something which we should bear in mind when considering observational constraints.

The 10 per cent–15 per cent relative difference in $\Delta\Sigma$ at $r_p \lesssim 1\,h^{-1}$ Mpc between the two models is roughly the same as the difference in $C_{\kappa\kappa}$ at $\ell \lesssim 2000$, but smaller than the difference in $C_{\kappa\kappa}$ at larger ℓ (see Fig. 2), and therefore we are interested in whether there is any difference in the signal-to-noise ratio (S/N) of these two probes. The S/N quantifies the distinguishability of the two models and is defined as

$$(\text{S/N})^2 \equiv [d_{F5}(x_i) - d_{GR}(x_i)]^T\, \mathbf{C}^{-1}(x_i, x_j)\, [d_{F5}(x_j) - d_{GR}(x_j)]\,, \tag{32}$$

in which x_i is the data in the ith bin ($x = R_p$ for GGL and $x = \ell$ for lensing convergence), and $\mathbf{C}$ is the covariance matrix.

To estimate the S/N values, we consider three fiducial surveys with roughly the DES, HSC, and LSST specifications, as summarized in Table 3. We expect that Euclid will have a similar performance

---

[4] This is a slight abuse of notation, but it should be clear, given the context, where z means the los coordinate or redshift.

Table 3. The three hypothetical lensing surveys used to estimate the statistic error for galaxy–galaxy weak lensing and the convergence power spectrum. n_{gal} is the source galaxy number density (the sources are assumed to be at $z_{source} = 1.0$ in all cases), and σ_{int} the intrinsic ellipticity of sources. For GGL, we have assumed the lens galaxies are at $z_{lens} = 0.30$.

Hypothetic survey	n_{gal} (arcmin^{-2})	σ_{int}	Survey area (deg^2)
DES	3	0.35	5000
HSC	30	0.35	1400
LSST	50	0.35	20 000

as LSST (see e.g. Cautun et al. 2017, for some relevant S/N analysis but for void lensing using Euclid and LSST). For simplicity, let us assume that there are overlapping spectroscopic surveys which can provide galaxy catalogues with a number density at least as high as the ones used in our lensing galaxies, between $0.16 \lesssim z \lesssim 0.43$. As shown above, the model difference in $\Delta\Sigma(r_p)$ is insensitive the lens redshift, so we assume a single lens redshift $z_{lens} = 0.3$ and a single source redshift $z_{source} = 1$ in the simplified study. The covariance matrix **C** is calculated based on a halo model prescription following Jeong, Komatsu & Jain (2009), which accounts for contributions from cosmic variance, the Poisson noise of lensing galaxies and the shape noise of source galaxies, and it adopts single source and lens redshifts as was mentioned above. The GR HOD and cosmological parameters for the snapshot at $z \sim 0.3$ are used to generate **C**. We also adopt the halo-model approach developed in Sato et al. (2009) to estimate the covariance matrix for $C_{\kappa\kappa}$. In this matrix, we properly include the non-Gaussian term induced by convergence tri-spectrum and halo sample variance.

Fig. 7 shows the S/N based on our analysis which takes into account statistical uncertainties only, for the GGL (left-hand panel)
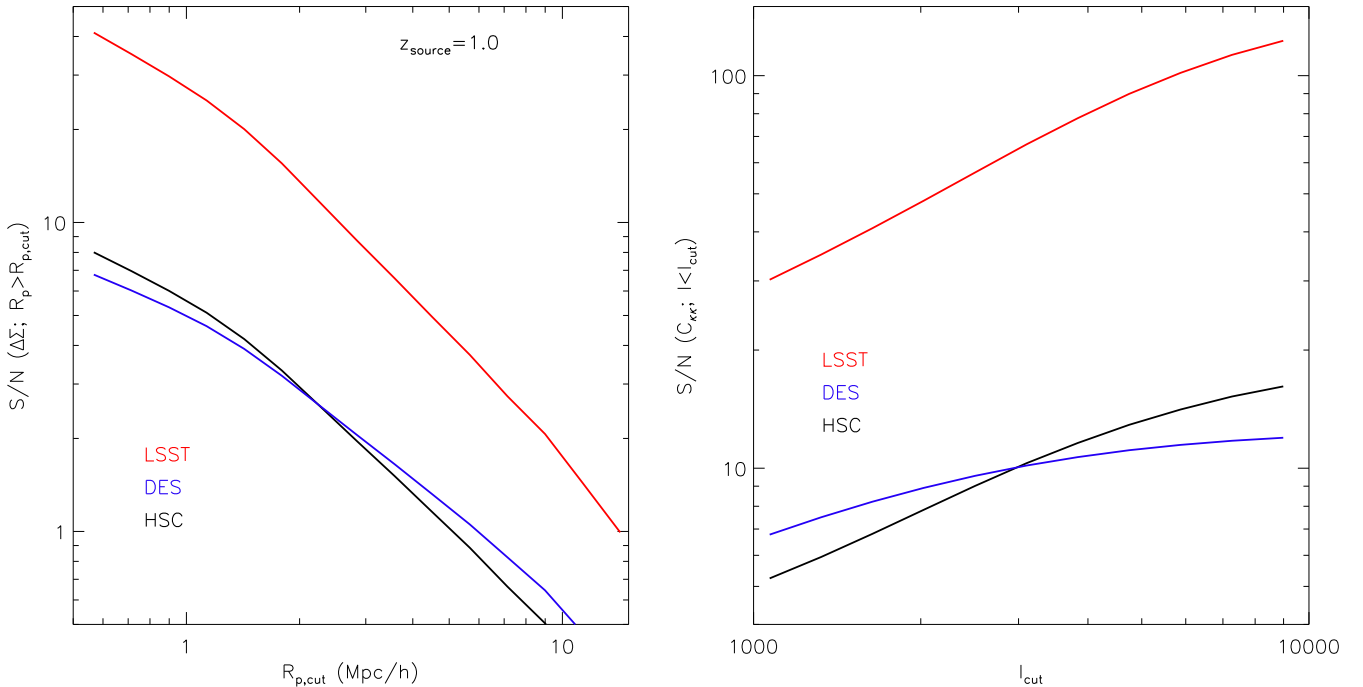
and $C_{\kappa\kappa}$ (right-hand panel). The black, blue, and red curves are, respectively, for HSC, DES, and LSST-like surveys. In the case of GGL, we show S/N as a function of the minimum r_p used in the calculation, while for the case of $C_{\kappa\kappa}$ the S/N is displayed as a function of the maximum ℓ included in the analysis. These are because using a smaller (larger) cut-off in r_p (ℓ) means more data are included in the model test, which can increase the S/N; but on the other hand, by doing these we are moving to smaller scales, where we would need to worry about other theoretical uncertainties such as the impact of baryons. Eventually, a comprise between these two considerations will have to be made; but for this study we are mainly interested in how the S/N values vary with the r_p and ℓ cuts.

From Fig. 7, we can see that LSST, being a stage-4 experiment, has significantly more power to distinguish the two models, thanks to its larger sky coverage and higher source galaxy number density; this is true for both GGL and $C_{\kappa\kappa}$. HSC and DES, both of which are stage-3 experiments, show similar performances. When comparing the two probes, we find that $C_{\kappa\kappa}$ gives larger S/N values for all three surveys – this is not surprising as both can be symbolically written as $\langle AB \rangle$ where A, B are two statistics of the underlying density field and $\langle \cdot \rangle$ denotes ensemble average. For $C_{\kappa\kappa}$, $A = B = \kappa$, while for GGL we have $A = \kappa$ and $B = \delta n_g$, where δn_g is the galaxy number density fluctuation, the model difference in which has been greatly reduced by the tuning of HOD parameters. Therefore, we expect the model difference in GGL to be smaller than that in $C_{\kappa\kappa}$.

3.2.3 Effect of tracers

Because the galaxy–matter cross-correlation quantifies the distribution of matter around galaxies, the choice of galaxies is important, which is why we made effort to tune the HOD parameters in the F5
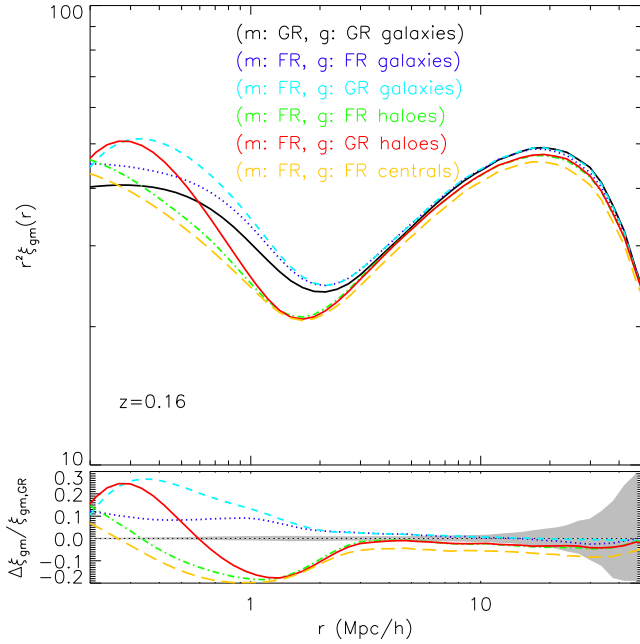

Figure 7. Left-hand panel: the S/N, defined in equation (32), from GGL as a function of $R_{p,cut}$, which is the minimum projected radius R_p used in the calculation. $R_{p,max} = 25 \, h^{-1}$ Mpc here and the model differences are calculated using the results from the $L_{box} = 450 \, h^{-1}$ Mpc simulations. The black, blue, and red curves are the results by using the covariance matrices for the assumed HSC, DES, and LSST surveys, respectively. Right-hand panel: the S/N from the lensing convergence power spectrum as a function of the maximum ℓ (ℓ_{cut}) used in the analysis, with $\ell_{min} = 200$. The colours of the curves are the same for the left-hand panel.

Figure 8. Top panel: ξ_{gm} for different choices of tracers to cross-correlate with matter. The black solid curve is the cross-correlation between HOD galaxies and dark matter both from the GR $L_{box} = 900\,h^{-1}$ Mpc simulation, while the other curves are cross-correlations of dark matter from the F5 simulation with a variety of choices of tracers – HOD galaxies for the F5 simulation (blue dotted), HOD galaxies for GR (cyan dashed), dark matter haloes for F5 (green dot–dashed), haloes for GR (red dot-dot-dot–dashed) and central HOD galaxies for F5 (orange long dashed). In the cases of haloes being the tracers, the haloes are ranked from high to low mass and the first $\bar{n}_{g,GR} L_{box}^3$, where $\bar{n}_{g,GR}$ is the averaged HOD galaxy number density from the GR simulation at $z = 0.16$, are used. Bottom panel: the relative differences between the other cases and the ξ_{gm} for GR galaxies and dark matter, with the same line styles and colours as in the top panel. The yellow shaded region shows the 68 per cent scatter of the 125 Jackknife resamples around the mean, for the cross-correlation between galaxies and dark matter in GR.

case to match the 3D galaxy two-point correlation function ξ_{gg} (and the galaxy number density) in the two models. To gain a feeling of the effect of choosing different tracers of the matter field, we have, for the snapshot at $z = 0.16$[5] of the $L_{box} = 900\,h^{-1}$ Mpc simulation, tested how ξ_{gm} changes by using other tracers. The result is shown in Fig. 8 (see the figure caption for a more detailed description of the different curves). There are several interesting features in this figure.

First of all, we see that at small separations ξ_{gm} is indeed very sensitive to the choice of tracers, as expected. The difference caused by this is substantially larger than that between F5 and GR as we have show above. Evidently, for the one-halo term of ξ_{gm}, changing the tracer is equivalent to placing the tracer to a different location in its host halo, or even outside the halo, which can impact the matter distribution around. This sensitivity is reduced at large separations, at which the effect of slightly relocating the tracer is smaller.

Second, for the two cases of cross-correlating dark matter distribution from the F5 simulation with haloes (green dot–dashed and red dot-dot-dot–dashed), the lowest points in the curve shift to-

---

[5] We only use one snapshot because, as we have seen above, the model difference between F5 and GR shows little redshift evolution in the redshift range considered in this paper.

wards smaller separations, and ξ_{gm} is overall lower than the cross-correlations by using HOD galaxies. Using haloes as tracers is similar to using only the central galaxies, and misses the contribution from satellite–matter cross-correlation, which may have caused this feature. To check this, we show the result of cross-correlating the dark matter field with only the central HOD galaxies, in the case of F5, as the orange long dashed curve in Fig. 8. The behaviour is very similar to the cross-correlation with haloes, and the slight difference is because the two tracer classes do not correspond to exactly the same halo population, since central galaxies are populated in haloes in a random way.

Third, for the two cases in which we cross-correlate the dark matter field from the F5 simulation with tracers from the GR simulation (cyan dashed and red dot-dot-dot–dashed), ξ_{gm} decreases towards very small separations ($r \lesssim 0.3\,h^{-1}$ Mpc), and this is because GR tracers usually do not coincide with the highest density peaks in the dark matter field of the F5 simulation so that the highest values of ξ_{gm} appear to be away from the GR tracers themselves.

All in all, the test highlights the importance of using carefully constructed mock galaxy catalogues when we compare the predictions of GGL in different models. As an example, the 3D real-space two-point correlation functions and the projected 2D correlation functions in our GR and F5 HOD catalogues agree with each other within 2 per cent–3 per cent in the range of separations considered here, but such agreements are in a statistical, rather than an object-by-object, sense. When cross-correlated with the same (F5) matter field, the ξ_{gm} results by using F5 and GR galaxies are indeed different (cf. blue dotted and cyan dashed curves in Fig. 8), in particular at small separations. This indicates that high-resolution simulations enable to accurately resolve the internal structures of haloes and to allow realistic galaxy mocks to be constructed, are necessary in order to make GGL more useful for distinguishing f(R) gravity and GR.

3.3 Galaxy bias

Finally, we compare the galaxy biases in GR and f(R) gravity. We are interested in this comparison this for two reasons.

First, in standard ΛCDM, the linear bias factor, defined as

$$b_{lin}(r) = \frac{\xi_{gm}(r)}{\xi_{mm}(r)} = \frac{\xi_{gg}(r)}{\xi_{gm}(r)} = \sqrt{\frac{\xi_{gg}(r)}{\xi_{mm}(r)}}, \qquad (33)$$

is scale-independent on large scales. On the other hand, it is known that f(R) gravity, and in general chameleon models, predict a scale-dependent linear growth rate of matter density perturbations, which may result in scale-dependent b_{lin}, because we have tuned the HOD parameters to match $\xi_{gg}(r)$ in the two models, while their $\xi_{mm}(r)$ can have a scale-dependent difference. We want to check whether, at least for F5, such a scale dependence of b_{lin} is significant enough to make it of interest in observations.

Secondly, assuming that the linear bias factor b_{lin} gives a correct quantification of galaxy bias at some given scale r, the galaxy–matter cross-correlation coefficient R_{gm}, defined as

$$R_{gm}(r) \equiv \xi_{gm}(r)/\sqrt{\xi_{gg}(r)\xi_{mm}(r)}, \qquad (34)$$

is equal to 1. This offers an opportunity to derive the matter correlation function ξ_{mm} from observational determinations of ξ_{gg} and ξ_{gm}. We want to see whether the minimum length-scale R_{min} above which this can be performed without worrying about the non-linear effects in galaxy bias is significantly different in GR and in F5.
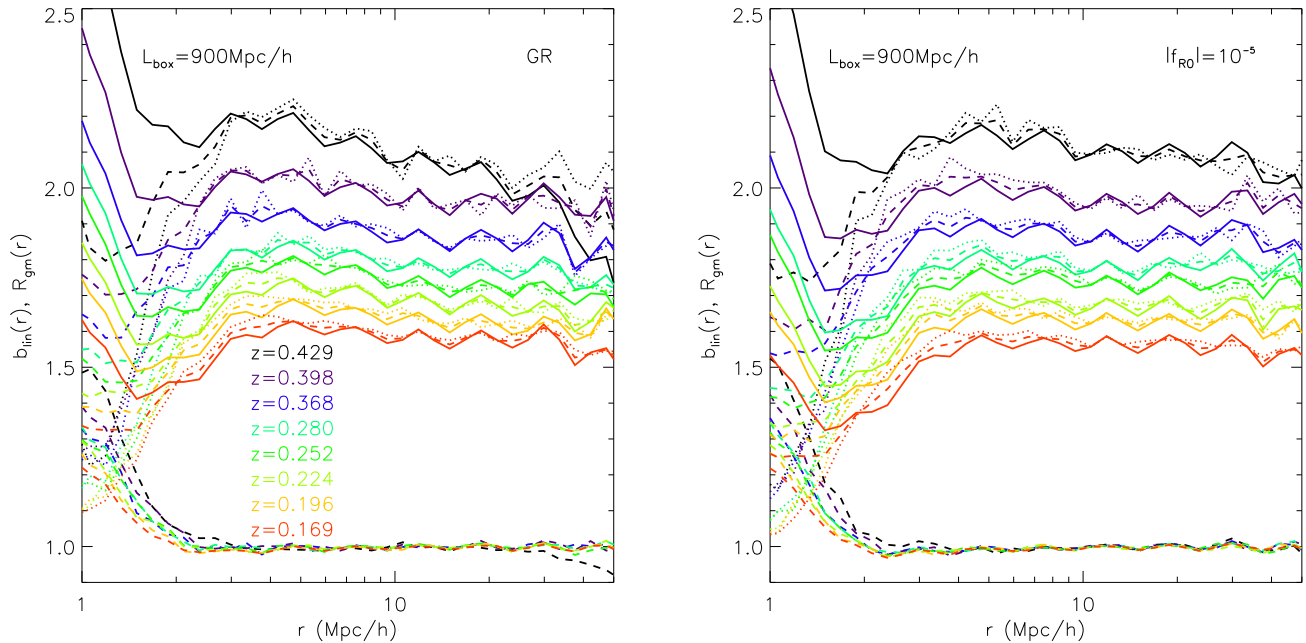
Figure 9. Left-hand panel: the bunch of curves on the top of the panel show the linear galaxy bias defined in three ways – $b_{\rm lin} \equiv \xi_{\rm gm}/\xi_{\rm mm}$ (solid), $b_{\rm lin} \equiv \sqrt{\xi_{\rm gg}/\xi_{\rm mm}}$ (dashed), and $b_{\rm lin} \equiv \xi_{\rm gg}/\xi_{\rm gm}$ (dotted) – from the GR $L_{\rm box} = 900\,h^{-1}$ Mpc simulation. The redshifts of the curves are given in the legend, using the same colour scheme and order (from top to bottom) as the curves themselves. The dashed lines at around 1.0 are the galaxy–matter correlation coefficient defined as $R_{\rm gm} \equiv \xi_{\rm gm}/\sqrt{\xi_{\rm gg}\xi_{\rm mm}}$ for the same redshifts. Right-hand panel: the same as the left-hand panel, but for F5.

Fig. 9 shows the results of our tests to answer these questions. The top bunch of curves in each panel (left for GR and right for F5) show the linear bias factors calculated in different ways (the different line styles) at a selection of redshifts (shown by different colours; see the legend for more details). We see that the different ways of calculating $b_{\rm lin}$ agree well with each other, and that $b_{\rm lin}$ remains roughly constant down to $r \sim 4\,h^{-1}$ Mpc, in agreement with previous results (e.g. Yoo et al. 2006). This holds true for all redshifts and both models – the latter is perhaps not surprising given that $\xi_{\rm gg}$ has been tuned to match in GR and F5, while $\xi_{\rm gm}$ in these models differ by at most a few per cent above $r \sim 4\,h^{-1}$ Mpc, so that any scale dependence of $b_{\rm lin}$ should be very weak. Note that $b_{\rm lin}$ is larger at higher redshifts, since the number densities of galaxies are lower for those redshifts and so we are looking at more biased tracers of the underlying matter field.

The results of $R_{\rm gm}$ are shown as dashed lines near the bottom of the left-hand (right-hand) panel for GR (F5), for the same redshifts and using the same colour scheme. We can see that for r down to 1–$2\,h^{-1}$ Mpc $R_{\rm gm}$ is equal to unity to a good accuracy, and there is no significant difference between the different redshifts or between GR and F5. This suggests that the reconstruction of $\xi_{\rm mm}$ from $\xi_{\rm gg}$ and $\xi_{\rm gm}$ can be done with the same reliability whether the underlying model is GR or F5 – this is even with the consideration that $b_{\rm lin,F5}$ may vary by a few per cent (in theory) from vary large scales to $r \sim 4\,h^{-1}$ Mpc.

4 SUMMARY AND DISCUSSION

We have studied the possibility of using galaxy–galaxy weak lensing to distinguish between the standard ΛCDM paradigm and a lead alternative, chameleon $f(R)$ gravity. The parameter for the latter is chosen so that the model is not yet firmly ruled out by cosmological data. The study can also lead to a more quantitative assessment of to what accuracy deviations – in the way as prescribed by chameleon

type theories – from GR on cosmological scales can be constrained by future GGL observations. To this end, we have decided to make accurate theoretical predictions for a representative MG model, by the means of fully non-linear N-body simulations.

We take a step further by carefully making appropriate galaxy catalogues in order to predict the GGL signals for both ΛCDM and $f(R)$ gravity. The reason is this: while the $f(R)$ model studied here has a stronger gravitational interaction than in GR, and thus would predict more dark matter haloes and an enhanced large-scale clustering, the lack of a reliable predictive model for galaxy–halo connection means that we cannot rule out it on the basis of its predicted galaxy clustering using some approximate method. Hence, we follow a more pragmatic approach, by assuming that both models produce an acceptable galaxy clustering (as required by observations), and focusing only on the resulting lensing effect. In practice, this is achieved by adopting the HOD prescription of galaxy–halo connection, and tuning the HOD parameters in the $f(R)$ model to match the galaxy clustering in its ΛCDM counterpart. We have checked explicitly, e.g. in Fig. 8, that the choice of tracers (the galaxy catalogues) has a non-negligible effect on the resulting GGL signal.

Before looking at GGL, we have first inspected the weak lensing convergence power spectrum in the selected $f(R)$ model. This has been studied before, but here we focus on the connection to the matter power spectrum and its time evolution. Fig. 3 is a useful plot to understand how much contribution the convergence power spectrum has received from the matter clustering at different scales and epochs. We have checked that the behaviour of the former can be qualitatively explained using the latter.

Compared to the convergence and matter power spectra, which quantify the autocorrelation of the matter density field, we find that the cross-correlation between galaxies and matter, $\xi_{\rm gm}(r)$, shows a $\sim$50 per cent smaller difference between the two model studied, because the galaxy clustering in these models has been tuned to

agree well with each other. This is further verified by an analysis of the S/N, which quantifies the distinguishability of the models when statistical-only errors are used, for three imaging surveys similar, respectively, to the DES, HSC, and LSST specifications, with synergy data from a spectroscopic survey that can at least match the BOSS LOWZ galaxy number density at $0.16 \lesssim z \lesssim 0.43$. We find that the S/N is smaller than 2–3 for DES and HSC, if we exclude GGL data within 2–$3\,h^{-1}$ Mpc, while for the LSST-like survey we have S/N ~ 10. The S/N is 2–4 times higher if the cosmic shear power spectrum, with a conservative cut at $\ell_{\min} = 1000$–2000, is used for constraints. In the redshift range covered in this study, we do not find any strong dependence of the model difference in GGL on the lens redshift – indeed, Fig. 6 shows that the low-z and high-z samples give almost identical results.

Note that in the above forecast, we have included only statistical and not systematic uncertainties. Although the cosmic shear power spectrum can have a higher S/N than GGL for distinguishing $f(R)$ gravity, it still remains useful and complementary to consider GGL. Current two-point correlation analysis of cosmic shear is subject to observational systematics induced by imperfect measurement of distant galaxies. The multiplicative bias is one of the most important systematics in cosmic shear analysis and can make the amplitude of lensing power spectrum uncertain (e.g. Huterer et al. 2006). In recent cosmological analyses, the impact has been controlled by image simulations (e.g. Hildebrandt et al. 2017) or appropriate parametrization (e.g. DES Collaboration 2017). On the other hand, GGL analysis can separate the multiplicative bias and lensing effects from observed signal if one can use single-source population and multiple foreground objects at different redshifts (Oguri & Takada 2011). We also note that the intrinsic alignments of galaxy ellipticities, which are a significant source of systematic errors for cosmic shear measurements (e.g. Hirata & Seljak 2004), are not important for GGL with single-source population. This is because the stacked lensing is linear in shear, and does not include any correlation between the shapes of different galaxies.

We have investigated galaxy bias in the ΛCDM and $f(R)$ models. It is well known that $f(R)$ gravity models have scale-dependent linear growth rate, that goes back to the ΛCDM prediction on large scales. Fig. 4 is an example of this scale dependence, although it shows the non-linear growth of matter density perturbations. Hence, we expect the linear galaxy bias to be different in these two models. However, from Fig. 9, we do not find a clear difference: the different values at the different redshifts are more likely due to the different corresponding galaxy number densities, as we know that the more luminous galaxies (for which n_g is smaller) are more strongly biased tracers of the dark matter field. The F5 galaxy bias, at a given redshift, only shows a rather weak scale dependence and is slightly smaller than the GR value, the latter being because ξ_{gg} is tuned to agree in the two models while ξ_{mm} is larger in $f(R)$ gravity. On the other hand, we find that, as in GR, the galaxy–mass cross-correlation coefficient R_{gm} remains at 1.0 down to $\sim 3\,h^{-1}$ Mpc, suggesting that one can infer ξ_{mm} from measurements of galaxy auto correlation and GGL at scales larger than $\sim 3\,h^{-1}$ Mpc.

As a first study of GGL in $f(R)$ gravity, this work can be further improved in several ways, all of which require more (and more advanced) simulations than used here.

First, as shown in Fig. 5, the galaxy–mass cross-correlation ξ_{gm} (and therefore GGL) depends sensitively on the number density of lenses. Our galaxy catalogues are made to mimic the BOSS LOWZ sample, with a number density of order $10^{-4}(h^{-1}$ Mpc$)^{-3}$, and this number will be further increased with ongoing and future galaxy surveys. It remains interesting to see how effectively the

increased lens number density can help improve the S/N, given that many of the newly added galaxies will be fainter. In order to check this, we will need simulations with higher resolutions to populate fainter galaxies, and such simulations may also enable mock galaxy catalogues constructed using other techniques such as SHAM and SAM, to understand the impact of different methods of galaxy–halo connection.

In relation to the above point, one might wonder if the differences in the GGL signals of F5 and GR are actually due to the fact that, even after the tuning of HOD parameters, F5 catalogues generally still have more (up to 4 per cent as shown in Fig. 1) galaxies than in GR. To check this possibility, we have used a set of five independent realizations (with different initial conditions) of GR and F5 simulations ($L_{box} = 1024\,h^{-1}$ Mpc and $N_p = 1024^3$) to make HOD catalogues using the same method as prescribed in this paper, and studied their respective GGL signals. In these catalogues, F5 have 0.8 per cent–2.4 per cent (<4 per cent) more galaxies than GR. We do not find any correlation between how many more galaxies F5 has than GR and how much the GGL signal in F5 is stronger than in GR, and we find the same enhancement of GGL in F5 as in this paper. Therefore, we conclude that the slight difference of the HOD galaxy numbers in our F5 and GR galaxy catalogues does not have a strong impact in the use of GGL to constrain F5. This is as expected, because the enhancement of matter clustering around galaxies is a physical consequence of MG.

Second, the simulations used here are for a choice of particular cosmological parameters (*WMAP9*). It is important to understand whether other choice of cosmological parameters can have a significant impact on the model difference in GGL. It is also important to check if there is a degeneracy between MG and cosmology, e.g. whether the effect of $f(R)$ gravity can be mimicked by a different value of σ_8 or Ω_m, as such a degeneracy can downgrade the potential of using GGL to constraint chameleon $f(R)$ models. For example, it was shown (Yoo et al. 2006) that the GGL signal $\Delta\Sigma(r_p) \propto \Omega_m^\alpha \sigma_8^\beta$, with α, β depending weakly on r_p, and therefore it is possible that the r_p-dependence of $\Delta(\Delta\Sigma)/\Delta\Sigma_{GR}$ is not completely degenerate with the effects of varying Ω_m and σ_8, allowing these different parameters to be constrained simultaneously using GGL alone, or possible synergies of GGL with other probes. This will require simulations with different cosmologies.

Third, in the forecast above, we have deliberately not used signals on smaller scales ($R_r \lesssim 2$–$3\,h^{-1}$ Mpc and $\ell > 1000$–2000), not just for resolution consideration, but also to be conservative as on those scales the theoretical predictions might be significantly affected by poorly understood baryonic physics (which is not included in the simulations used in this work). The modified gravitational force can change the halo density profiles, which is reflected in the GGL signals. However, to reliably include this in the model test, we have to fully understand how baryonic processes affect the (re)distribution of matter inside dark matter haloes for $f(R)$ gravity, and for this hydrodynamical simulations with suitably adjusted subgrid physics are essential. This is an almost entirely unexplored regime to date.

REFERENCES

Aihara H. et al., 2017, Publ. Astron. Soc. Japan, preprint (arXiv:1704.05858)
Alonso D., 2012, preprint (arXiv:1210.1833)
Arnold C., Puchwein E., Springel V., 2014, MNRAS, 440, 833
Barreira A., Cautun M., Li B., Baugh C. M., Pascoli S., 2015a, J. Cosmol. Astropart. Phys., 08, 028
Barreira A., Li B., Jennings E., Merten J., King L., Baugh C. M., Pascoli S., 2015b, MNRAS, 454, 4085
Barreira A., Bose S., Li B., Llinares C., 2017, J. Cosmol. Astropart. Phys., 02, 031
Bartelman M., Schneider P., 2001, Phys. Rep., 340, 291
Behroozi P. S., Wechsler R. H., Wu H., 2013, ApJ, 762, 109
Berlind A. A. et al., 2003, ApJ, 593, 1
Bose S., Hellwing W. A., Li B., 2015, J. Cosmol. Astropart. Phys., 02, 034
Bose S., Li B., Barreira A., He J., Hellwing W. A., Koyama K., Llinares C., Zhao G., 2017, J. Cosmol. Astropart. Phys., 02, 050
Brainerd T. G., Blandford R. D., Smail I., 1996, ApJ, 466, 623
Brax P., van de Bruck C., Davis A.-C., Shaw D. J., 2008, Phys. Rev. D, 78, 104021
Cai Y., Padilla N., Li B., 2015, MNRAS, 451, 1036
Carroll S. M., de Felice A., Duvvuri V., Easson D. A., Trodden M., Turner M. S., 2005, Phys. Rev. D, 71, 063513
Carroll S. M., Duvvuri V. Trodden M., Turner M. S., 2004, Phys. Rev. D, 70, 043528
Cataneo M. et al., 2015, Phys. Rev. D, 92, 044009
Cautun M., Paillas E., Cai Y., Bose S., Armijo J., Li B., Padilla N., 2017, MNRAS, preprint (arXiv:1710.01730)
Ceron-Hurtado J. J., He J., Li B., 2016, Phys. Rev. D, 94, 064052
Clampitt J. et al., 2017, MNRAS, 465, 4204
Colombi S., Novikov D., 2011, Astrophysics Source Code Library, record ascl:1110.017
Crocce M., Pueblas S., Scoccimarro R., 2006, MNRAS, 373, 369
Dark Energy Survey Collaboration et al., 2016, MNRAS, 460, 1270
Deffayet C., Esposito-Farese G., Vikman A., Phys. Rev. D, 79, 084003
DES Collaboration et al., 2017, preprint (arXiv:1708.01530)
Dirian Y., Foffa S., Khosravi N., Kunz M., Maggiore M., 2014, J. Cosmol. Astropart. Phys., 06, 033
Gleyzes J., Langlois D., Piazza F., Vernizzi F., 2015, Phys. Rev. Lett., 114, 211101
Guzik J., Seljak U., 2002, MNRAS, 335, 311
Harnois-Deraps J., Munshi D., Valageas P., van Waerbeke L., Brax P., Coles P., Rizzo L., 2015, MNRAS, 454, 2722
Higuchi Y., Shirasaki M., 2016, MNRAS, 459, 2762

Hilbert S., Hartlap J., White S. D. M., Schneider P., 2009, A&A, 499, 31
Hildebrandt H. et al., 2017, MNRAS, 465, 1454
Hinshaw G. et al., 2013, ApJS, 208, 19
Hirata C. M., Seljak U., 2004, Phys. Rev. D, 70, 063526
Hoekstra H., Jain B., 2008, Ann. Rev. Nucl. Part. Sci., 58, 99
Hoekstra H., Yee H. K. C., Gladders M. D., 2004, ApJ, 606, 67
Hu W., Sawicki I., 2007, Phys. Rev. D, 76, 064004 (HS)
Hudson M. J., Gwyn S. D. J., Dahle H., Kaiser N., 1998, ApJ, 503, 531
Huterer D., Takada M., Bernstein G., Jain B., 2006, MNRAS, 366, 101
Ivezic Z. et al., 2008, preprint (arXiv:0805.2366)
Jeong D., Komatsu E., Jain B., 2009, Phys. Rev. D, 80, 123527
Joyce A., Jain B., Khoury J., Trodden M., 2015, Phys. Rep., 568, 1
Khoury J., Weltman A., 2004, Phys. Rev. D, 69, 044026
Kilbinger M., 2015, Rep. Prog. Phys., 78, 086901
Koyama K., 2016, Rep. Prog. Phys., 79, 046920
Lewis A., Challinor A., 2011, Astrophysics Source Code Library, record ascl:1102.026
Li B., Zhao G., Teyssier R., Koyama K., 2012, J. Cosmol. Astropart. Phys., 01, 051
Li B., Hellwing W. A., Koyama K., Zhao G., Jennings E., Baugh C. M., 2013, MNRAS, 428, 743
Liu X. et al., 2016, Phys. Rev. Lett., 117, 051101
Maggiore M., Mancarella M., 2014, Phys. Rev. D, 90, 023005
Mandelbaum R., Seljak U., Kauffmann G., Hirata C. M., Brinkmann J., 2006, MNRAS, 368, 715
Manera M. et al., 2017, MNRAS, 447, 437
Mota D. F., Shaw D. J., 2007, Phys. Rev. D, 75, 063501
Mummery B., McCarthy I. G., Bird S., Schaye J., 2017, MNRAS, 471, 227
Navarro J., Frenk C. S., White S. D. M., 1997, ApJ, 490, 493
Nicolis A., Rattazzi R., Trincherini E., 2009, Phys. Rev. D, 79, 064036
Oguri M., Takada M., 2011, Phys. Rev. D, 83, 023008
Osato K., Shirasaki M., Yoshida N., 2015, ApJ, 806, 186
Peirone S., Raveri M., Viel M., Borgani S., Ansoldi S., 2017, Phys. Rev. D, 95, 023521
Perlmutter S. et al., 1999, ApJ, 517, 565
Planck Collaboration XIII, 2016, A&A, 594, 13
Pratten G., Munshi D., Valageas P., Brax P., 2016, Phys. Rev. D, 93, 103524
Refregier A., 2003, ARA&A, 41, 645
Riess A. G. et al., 1998, ApJ, 116, 1009
Sato M., Hamana T., Takahashi R., Takada M., Yoshida N., Matsubara T., Sugiyama N., 2009, ApJ, 701, 945
Semboloni E., Hoekstra H., Schaye J., van Daalen M. P., McCarthy I. G., 2011, MNRAS, 417, 2020
Shirasaki M., Hamana T., Yoshida N., 2015, MNRAS, 454, 3043
Shirasaki M., Hamana T., Yoshida N., 2016, PASJ, 68, 4
Shirasaki M., Nishimichi T., Li B., Higuchi Y., 2017, MNRAS, 466, 2402
Smith R. E. et al., 2003, MNRAS, 341, 1311
Takakashi R., Sato M., Nishimichi T., Taruya A., Oguri M., 2012, ApJ, 761, 152
Tessore N., Winther H. A., Metcalf R. B., Ferreira P. G., Giocoli C., 2015, J. Cosmol. Astropart. Phys., 10, 036
Teyssier R., 2002, A&A, 385, 337
Wang J., Hui L., Khoury J., 2012, Phys. Rev. Lett., 109, 241301
Yoo J., Tinker J. L., Weinberg D. H., Zheng Z., Katz N., Dave R., 2006, ApJ, 652, 26
Zheng Z. et al., 2005, ApJ, 633, 791

This paper has been typeset from a TEX/LATEX file prepared by the author.